Neuronal phase- and amplitude-coupling in the healthy and diseased human brain

Dissertation

zur Erlangung des Grades eines

Doktors der Naturwissenschaften

der Mathematisch-Naturwissenschaftlichen Fakultät

und

der Medizinischen Fakultät

der Eberhard-Karls-Universität Tübingen

vorgelegt

von

Marcus Siems

aus Rostock, Deutschland

Tag der mündlichen Prüfung:	05.10.2022
Dekan der Math.-Nat. Fakultät:	Prof. Dr. Thilo Stehle
Dekan der Medizinischen Fakultät:	Prof. Dr. Bernd Pichler
1. Berichterstatter:	Prof. Dr. Markus Siegel
2. Berichterstatter:	PD Dr. Gabriele Lohmann
Prüfungskommission:	Prof. Dr. Markus Siegel
	PD Dr. Gabriele Lohmann
	Prof. Dr. Christoph Braun
	Prof. Dr. Andreas Bartels

Erklärung / Declaration:

Ich erkläre, dass ich die zur Promotion eingereichte Arbeit mit dem Titel:

“Neuronal phase- and amplitude-coupling in the healthy and diseased human brain”

selbstständig verfasst, nur die angegebenen Quellen und Hilfsmittel benutzt und wörtlich oder inhaltlich übernommene Stellen als solche gekennzeichnet habe. Ich versichere an Eides statt, dass diese Angaben wahr sind und dass ich nichts verschwiegen habe. Mir ist bekannt, dass die falsche Angabe einer Versicherung an Eides statt mit Freiheitsstrafe bis zu drei Jahren oder mit Geldstrafe bestraft wird.

I hereby declare that I have produced the work entitled “Neuronal phase- and amplitude-coupling in the healthy and diseased human brain”, submitted for the award of a doctorate, on my own (without external help), have used only the sources and aids indicated and have marked passages included from other works, whether verbatim or in content, as such. I swear upon oath that these statements are true and that I have not concealed anything. I am aware that making a false declaration under oath is punishable by a term of imprisonment of up to three years or by a fine.

Tübingen, ...

Datum / Date Unterschrift / Signature

Statement of contributions:

The first project “Dissociated neuronal phase- and amplitude-coupling patterns in the human brain” (Siems and Siegel, 2020) is a data-analysis project using publicly available data from the Human Connectome Project (HCP S900). The project was initiated to understand the empirical relationship between amplitude- and phase-coupling in the human brain. Marcus Siems conducted the study at the MEG Center Tübingen under the supervision of Prof. Dr. Markus Siegel. Markus Siegel and Marcus Siems jointly conceived the concept and scope of the study. Marcus Siems conducted the formal data analysis and wrote the original draft. Markus Siegel and Marcus Siems edited the manuscript to its final published form.

The second project “Altered cortical phase- and amplitude-coupling in Multiple Sclerosis” (Siems et al., 2021) was conducted to investigate the changes in amplitude- and phase-coupling in the diseased brain and compare these changes between the two coupling modes. It is a joint project between the MEG Center Tübingen, the Hertie Institute for Clinical Brain Research and the Department of Neurology & Stroke (Hertie) at the University of Tübingen. Dr. Johannes Tuennerhoff and Prof. Dr. Ulf Ziemann recruited the subjects and conducted the behavioral testing. Marcus Siems conducted the MEG measurements at the MEG Center Tübingen. Markus Siegel, Ulf Ziemann and Marcus Siems conceptualized the scope of the project. Marcus Siems lead the formal data analysis and conceived the multi-stage analysis pipeline to classify groups in high-dimensional feature-spaces, all under the supervision of Markus Siegel. Markus Siegel and Marcus Siems wrote the original manuscript draft included in this thesis.

Tübingen, ...

Date Signature

Table of Contents

Table of figures

Abstract

Oscillatory neuronal activity has been proposed to facilitate and multiplex the communication between distant brain regions. In particular, two key coupling modes have been discussed in this regard; amplitude- and phase-coupling between distant signals. Both can describe large-scale neuronal interactions independently of one another and have theoretically been linked to distinct neuronal mechanisms. However, to date the direct relations between functional networks derived from these two coupling modes remain unclear. In this thesis we conducted two magnetoencephalography (MEG) studies to empirically assess the relationship between amplitude- and phase-coupling networks in the healthy and diseased human brain.

In the first study we analyzed the publicly available human connectome project (HCP S900) dataset of 95 healthy subjects. We applied source-reconstruction to systematically compare cortical amplitude-coupling and phase-coupling patterns in the healthy human brain. We found significant similarities between amplitude- and phase-coupling patterns for almost the entire spectrum and cortex. We further showed that these patterns are similar but non-redundant, indicating a complex spatial and spectral distribution. By combining empirical measurements with simulations and attenuation correction, we sought to ensure that these results were not due to methodological biases but instead reflected relations between genuine amplitude- and phase-coupling, which may indicate at least partially distinct neuronal mechanisms. Additionally, we highlight and clarify the compound nature of amplitude-coupling of orthogonalized signals.

In our second study, we measured MEG in 17 relapsing-remitting Multiple Sclerosis patients at an early disease stage (median EDSS = 1.5, range 0 to 3.5) and 17 healthy controls to investigate brain-wide phase- and amplitude-coupling of frequency specific neuronal activity. We developed a new analysis approach that combines dimensionality reduction, bootstrap aggregating and multivariate classification to identify changes of brain-wide coupling in Multiple Sclerosis. We identified systematic and non-redundant changes of both phase- and amplitude-coupling. Changes included both, increased and decreased neuronal coupling in wide-spread, bilateral neuronal networks across a broad range of frequencies. These changes allowed to successfully classify patients and controls with an accuracy of 84%. Furthermore, classification confidence predicted behavioral scores of disease severity. Our results unravel systematic changes of large-

scale neuronal coupling in Multiple Sclerosis and suggest non-invasive electrophysiological coupling measures as powerful biomarkers of Multiple Sclerosis.

Overall, our two studies provide, to our knowledge, the first systematic analyses describing the relationship between amplitude- and phase-coupling networks. In both, the healthy as well as in the diseased brain, these two coupling modes are related but show distinguishable features. Our findings highlight that amplitude- and phase-coupling might at least partially originate from distinct neuronal mechanisms.

1 Introduction

Understanding cognition and the mechanisms of brain function are central goals of modern neuroscience. Over recent years the field has progressively shifted from a region-centered to a network centered view of brain function. A given task is most likely not solely solved by one specific brain area but rather the complex interplay of several regions (Biswal et al., 2010; Siegel et al., 2012; Singer, 1999). An increasing number of imaging tools have been deployed to assess such brain networks from a functional as well as a structural point of view. One branch of these brain-imaging techniques is electrophysiology. Here, electroencephalography (EEG), magnetoencephalography (MEG) and electrocorticography (ECoG) and corresponding analysis tools have been developed and improved to investigate brain function invasively (ECoG/LFP) and non-invasively (M/EEG). Their high temporal resolution makes them ideally suited to investigate dynamic neural processing and to bridge the gap between behavior and brain anatomy (Pesaran et al., 2018).

The temporally rich nature of electrophysiology yields several possibilities to analyze the interplay of distant brain regions for a variety of timescales. Prominent theories highlight the importance of rhythmic and spectrally band-limited oscillations to orchestrate effective timing and communication between distant neuronal assemblies (Engel et al., 2001; Fries, 2015; Singer, 1999). In such schemes, neuronal spiking activity is understood as a train of events following a periodic probability distribution, hence an oscillation (Destexhe et al., 1999; Fries, 2015; Jahnke et al., 2014; Jensen and Mazaheri, 2010). When an oscillatory generator is strong enough, these oscillations can be measured extra-cranially (Pesaran et al., 2018). Hereby, the defining features of an oscillation are the temporal distribution of its phase and amplitude. Over the last years a growing body of evidence has associated several aspects of cognition with spatially confined oscillatory activity (Donner and Siegel, 2011a; Engel et al., 2013; Siegel et al., 2012). These associations appear to be spectrally specific and have thus been coined “spectral fingerprints” (Siegel et al., 2012). Additionally, electrophysiological network measures have been increasingly used as a versatile biomarker for various neurological and psychiatric diseases (Fornito et al., 2015; Heuvel and Sporns, 2019; Stam, 2014).

1.1 Hypothesis

In this thesis we wanted to establish the relationship between amplitude- and phase-coupling networks. Despite the rapidly growing interest in these network measures and their increasing application in basic research and medical studies little is known about the relationship between phase- and amplitude-based networks. Amplitude-coupling describes the co-fluctuation of signal strengths and phase-coupling the consistent alignment of signals. These two features of large-scale neuronal interactions are in principle statistically independent (Bruns et al., 2000; Engel et al., 2013; Siegel et al., 2012) and represent two so-called coupling modes. Here, we report the findings of two MEG studies addressing the relationship between amplitude- and phase-coupling patterns in the healthy and the diseased human brain. We hypothesize that if amplitude- and phase-coupling are indeed related to two or more separate neuronal mechanisms, their network features should be dissociated as well. These studies are, to our knowledge, the first systematic analyses on this topic and establish several guidelines for the analyses of functional connectivity of non-invasive electrophysiological signals.

In our first study (Siems and Siegel, 2020), we analyzed 95 healthy subjects and computed amplitude- and phase-coupling for a broad range of frequencies. Several methodological obstacles impede the direct comparison of amplitude- and phase-coupling networks: First, MEG sensors as well as source-projected MEG signals are not independent. The superposition of electromagnetic fields in combination with the imperfect back-projection of the signal to the source space adds to the effect of volume conduction. Second, discounting volume conduction introduces spurious amplitude-coupling as a function of, among others, the underlying phase-coupling (Palva et al., 2018). Third, the measurement accuracy of functional connections, in other words the signal-to-noise ratio, affects the comparison of these networks. This is a problem because the power distribution in the brain is non-uniform over space (Hillebrand et al., 2012) as well as over frequencies (Voytek and Knight, 2015) and might induce false spatial or spectral specificity in our results.

Integrating these methodological issues into our guiding question we formulate the following hypotheses for our first study:

1.1) The measured amplitude-coupling networks cannot be fully explained by the spurious amplitude-coupling introduced from discounting volume conduction and thus at least partially reflect genuine amplitude-coupling.

1.2) Genuine amplitude- and phase-coupling patterns will be related but exhibit distinguishing features.

In our second study (Siems et al., 2021) we analyzed amplitude- and phase-coupling networks in both healthy controls as well as in a patient group. For this, we measured MEG of 17 relapsing-remitting Multiple Sclerosis (RRMS) patients at an early disease stage and 17 healthy controls. Multiple Sclerosis is a suitable disease model to analyze functional coupling changes as the disease mainly affects the brain's white matter. The goal of this study was to examine the differences in amplitude- and phase-coupling between healthy controls and patients. However, alterations to the anatomical connectome occur sparsely and diffusely in this early disease stage. One major problem that needs to be addressed is the variance between patients. Lesion locations will likely not overlap between subjects. Recent theories proposed that areas and connections higher up in the connectomic hierarchy, so-called hubs, might still show generalized effects (Fornito et al., 2015; Heuvel and Sporns, 2019; Stam, 2014). Hereby, it has been shown that neurological tissue damage does not solely lead to a lack or decrease of coupling but can as well show an increase in coupling as a result of compensatory effects.

Based on these assumptions we formulate the following hypotheses for our second study:

2.1) There exists a lower-dimensional feature space in which patient and control group can be classified.

2.2) The low-dimensional features will include both, amplitude- and phase-coupling, but will not be identical between the two coupling modes.

In the following we seek to give an introduction into the relevant literature forming the bedrock of each study. This includes in the first part a record of possible network measures, the mechanisms that are assumed to underlie amplitude- and phase-coupling and specific problems of non-invasive electrophysiology. In the second part of this thesis we introduce concepts and theories of functional coupling changes in the diseased human brain, focusing on Multiple Sclerosis. Hereby, the first part of this thesis corresponds to the published paper Siems and Siegel, 2020 and the second part is currently submitted for publication and a preprint is available under Siems et al., 2021.

2 Functional connectivity

The human brain is a highly complex and effective information transfer system. With approximately 100,000,000,000 neurons and one thousand connections per neuron, every neuron is connected with every other over maximally ~10 synapses (Herculano-Houzel, 2009; Kandel et al., 2000). This anatomical network constitutes the backbone of our conscious human experience and any behavioral output in general.

This structural organization has been linked to brain function throughout history. One of the first well-described and still valid functional networks involves the human language system and was first derived in the 19th century by Broca, Lichtheim and Wernicke from the analysis of lesioned patients (Geschwind, 1970, 1979; Poeppel et al., 2012; Wernicke, 1874). Their network view of brain function has survived until today.

With the proliferation of non-invasive brain imaging techniques the network view of brain function has been extended over the last decades. The term functional connectivity was coined to describe statistical relations between distant brain areas independent of their anatomical relations (for example Biswal et al., 2010; Friston, 1994). Importantly, these functional connections do not only form during the execution of a task but also during rest (for example Biswal et al., 1995; Raichle, 2015; Raichle et al., 2001).

Generally, anatomical connections are relatively stable over time, whereas functional connections change with task (Engel et al., 2013; Siegel et al., 2012), cognitive state (Dehaene and Changeux, 2011) as well as neuromodulatory regulation (van den Brink et al., 2019; Pfeffer et al., 2018). One handy metaphor for those two concepts, anatomical and functional connectivity, is of roads and traffic, respectively. The anatomical network defines a set of rules how information might travel between distant brain areas and functional connectivity describes the dynamic communication between those areas depending on external stimuli and internal states.

Over recent years, the study of resting-state functional connectivity focused on the correlation of functional magnetic resonance imaging (fMRI) time-courses. The systematic analysis of temporal relationships yielded several canonical networks, which appear to be stable over time and subjects (Biswal et al., 2010; Fox and Raichle, 2007; Smith et al., 2009; Yeo et al., 2011) and can be indicative of neurological and psychiatric disorders (for example Zhang and Raichle, 2010). However, the blood oxygen level-

dependent (BOLD) signal measured with fMRI is only a slow and indirect measure of neuronal activity (Logothetis, 2008). In contrast, electrophysiological signals, as for example measured with electroencephalography (EEG) and magnetoencephalography (MEG), directly measure the underlying neuronal activity. An additional advantage of M/EEG is its high temporal resolution, i.e. millisecond precision, which increases the sensitivity to fast changes of activity and opens a window to the rich spectral dynamics of neuronal activity (Siegel et al., 2012). Narrow-band as well as oscillatory activity interactions can define large-scale neuronal networks beyond BOLD signal correlations (Hipp and Siegel, 2015) and might provide new insights into circuit level mechanisms of neuronal organization (Donner and Siegel, 2011a; Engel et al., 2013; Siegel et al., 2012).

2.1 Electrophysiological coupling modes

In non-invasive human electrophysiology two fundamental features can be used to obtain functional connectivity networks: The amplitude and the phase of the signal. Functional connectivity derived from the amplitude of two or more signals is defined as the co-fluctuation of signal strengths. Phase-coupling on the other hand reflects the consistent temporal alignment of the phases of two or more signals.

These two concepts are theoretically independent and lay the foundation for several coupling measures. These measures can be broadly classified by four categories: directed vs. undirected, bivariate vs. multivariate, linear vs. non-linear and static vs. dynamic coupling (for an overview, cf.: Colclough et al., 2016; van Diessen et al., 2015; Marzetti et al., 2019; Zhigalov et al., 2017). In the current studies we mainly focused on undirected, bivariate, linear, static measures of coupling.

The neuronal mechanisms of phase- as well as amplitude-coupling are yet to be fully understood (Engel et al., 2013; Siegel et al., 2012) and direct evidence of relationships between these coupling modes is scarce (Avramiea et al., 2021; Daffertshofer et al., 2018; Mehrkanoon et al., 2014). Phase-coupling has been proposed to foster effective communication between neuronal assemblies (Fries, 2015; Womelsdorf et al., 2007). The so-called “communication through coherence” hypothesis suggests that neuronal assemblies exhibit periodic excitation-inhibition cycles and hence are more susceptible to spiking input at certain time points within the cycle. Effective communication is granted when the assembly gets input time-locked to the excitable phase of the cycle.

This mechanism would, on the macroscopic level, generate two frequency specific phase-coupled signals (Fries, 2015). Accordingly, phase-coupling has been associated with performance in various cognitive domains including selective attention (Bosman et al., 2012; Buschman and Miller, 2007; Siegel et al., 2008), perception (Hipp et al., 2011a), memory (Fell and Axmacher, 2011; Palva et al., 2010a, 2010b) and task-switching (Buschman et al., 2012).

Amplitude-coupling on the other hand refers to the temporal co-modulation of the amplitude (or power) of neuronal oscillations. Like phase-coupling, amplitude-coupling may not only result from, and thus reflect, neuronal interactions, but may also regulate these interactions by temporally aligning distant processes associated with fluctuating oscillations (von Nicolai et al., 2014; Siegel et al., 2012). Amplitude-coupling is also expressed in well-structured cortical networks that match known anatomical and functional connectivity (Hipp et al., 2012; Siems et al., 2016), resemble fMRI correlation patterns (Boto et al., 2021; Brookes et al., 2011; Deco and Corbetta, 2011; Destexhe et al., 1999; Hipp and Siegel, 2015; Mantini et al., 2007; Nir et al., 2008; O'Neill et al., 2015), and are more stable than phase-coupling networks (Colclough et al., 2016; Wang et al., 2014). Amplitude-coupling is largely driven by amplitude dynamics below 0.1 Hz (Hipp et al., 2012; Leopold et al., 2003). Hypothetically, the slow dynamics of amplitude-coupling may reflect the general establishment and decay of communication channels (Destexhe et al., 1999; Engel et al., 2013; Larson-Prior et al., 2011; Leopold et al., 2003; von Nicolai et al., 2014). A coincidence of high amplitudes in distant brain areas, i.e. high excitability in both areas, can promote effective direct communication. Analogously, recent studies linked neuromodulatory brainstem activity with intrinsic signal co-fluctuations (compare van den Brink et al., 2019; Pfeffer et al., 2020). This association indicates a possible mechanism for slow connectivity dynamics, for example via noradrenergic modification of the excitation-inhibition balance in local neuronal circuits (Froemke, 2015; Pfeffer et al., 2018, 2020).

Beyond their proposed dissociations, some studies identified strong relationships between amplitude- and phase-coupling. One study found that phase-coupling between areas in conjunction with local cross-frequency phase-amplitude coupling within areas might induce amplitude-coupling between areas (von Nicolai et al., 2014). Similarly, a novel modeling approach found that directed communication between brain areas can stem from rhythmic synchronization within a sending area propagated through

anatomical connections (Schneider et al., 2020). Within this framework both phase- and amplitude-coupling might originate from such directed communication channels. Moreover, Womelsdorf and colleagues (2007) have shown that strong amplitude-coupling can be related to particular phase relations between neuronal assemblies (Womelsdorf et al., 2007). It is therefore plausible that amplitude- and phase-coupling share features in their respective network architecture. This relationship between amplitude- and phase-coupling was the focus of our first study (Siems and Siegel, 2020). We proposed that if both coupling modes arise from different neuronal mechanisms the derived networks would diverge.

2.2 Challenges of electrophysiological connectivity measures

The functional mapping of brain activity offers great potential in understanding the mechanisms of neuronal processing non-invasively. However, no single imaging procedure can claim the status of a gold standard. M/EEG data has the advantage of measuring brain activity directly with a high temporal resolution, but there are several caveats that have to be considered when applying these measurement modalities.

First, M/EEG measures the superposition of neuronal electro-magnetic activity on the scalp level (Baillet et al., 2001) with the sensors being far away from the neuronal activity. Thus, every sensor picks up activity not only from tissue directly underneath it but a compound signal of all possible sources. Defining neuronal generators of activity from the sensor level data is one of the major challenges in non-invasive electrophysiology and is coined the inverse problem. Due to the poor signal-to-noise ratio of scalp-recordings, the limited number of sensors and the almost infinite number of possible generator configurations there is no analytic and definite solution; the inverse problem is mathematically ill-posed. Therefore, every source reconstruction is solely an estimation guided by assumptions on, for example, anatomy (Pascual-Marqui et al., 2002, 2011) or unit-gain constraints (spatial filtering; Gross et al., 2001; Van Veen et al., 1997). Thus, the spatial resolution of M/EEG source analyses is considerably lower as compared to fMRI for example.

Second, as a consequence of imperfect source-estimation and the super-position of electromagnetic fields, estimated sources are not independent measures of neuronal activity. Thus, functional connectivity as a statistical measure of interactions between signals will be positively offset. These volume conduction effects lead to spurious and

trivial connectivity patterns and potentially mask physiologically relevant networks (Hipp et al., 2012). As a consequence several network measures have been developed to address the problem of signal leakage (for example Brookes et al., 2011; Hipp et al., 2012; Nolte et al., 2004, 2020; Pascual-Marqui, 2007; Stam et al., 2007; Vinck et al., 2011). Their foundation is that electric and magnetic signals travel and superimpose virtually instantaneously and affect different sensors and estimated sources with zero phase delay (Nolte et al., 2004). However, true physiological interactions can display any phase shift, due to, for example, variable conduction delays between neuronal assemblies.

Two classes of algorithms have been developed to discount volume conduction: signal orthogonalization and removing the real component of the cross-spectrum (Brookes et al., 2011; Hipp et al., 2012; Nolte et al., 2004; Stam et al., 2007; Vinck et al., 2011), mainly applied to amplitude- and phase-coupling, respectively. Both methods remove the signal components that exhibit zero phase delay between paired signals. Signal orthogonalization sets the phase relation between two signals at any time point to 90 degrees, effectively removing volume conduction effects (Brookes et al., 2012; Hipp et al., 2012). Thus, this procedure destroys almost all phase relations between the signals. Conversely, assessing only the imaginary component of the cross-spectrum leaves the phase relations interpretable but removes any interaction that can be affected by the zero-lagged volume conduction effect.

3 Dissociated neuronal phase- and amplitude-coupling patterns in the human brain

3.1 Scientific questions and aims

In our first project we addressed whether different coupling modes, i.e. amplitude- and phase-coupling, can be dissociated (Siems and Siegel, 2020). Recent research on functional connectivity of electrophysiological signals mainly focused on the meticulous description of each coupling mode separately. However, a systematic framework to compare these measures empirically is still missing and many questions remain unanswered. For instance, do patterns of amplitude- and phase-based connectivity measures differ? Little is known about their empirical relationship (Bruns et al., 2000; Leopold et al., 2003) but this question is of major importance due to the potentially different neuronal origins these coupling modes indicate (Engel et al., 2013; Siegel et al., 2012).

As straightforward as this comparison appears its empirical investigation is non-trivial. Several obstacles impede a direct comparison of amplitude- and phase-based functional connectivity. Non-neuronal signal components, i.e. muscle, ocular and cardiac activity as well as volume conduction, have to be discounted. Any form of artifactual component might bias the similarity, predominantly towards overestimating the relationship (Hipp and Siegel, 2013; Hipp et al., 2012). Additionally, discounting volume-conduction by signal orthogonalization introduces spurious amplitude-coupling as a function of, among others, the strength of the underlying phase-coupling (Palva et al., 2018). In other words, the measured amplitude-coupling reflects a mixture of genuine amplitude-coupling of interest and spurious amplitude-coupling due to phase-coupling.

Thus, we tried to answer two main questions in this study taking all of the above-mentioned methodological issues into account. First, we tested if we can identify genuine amplitude-coupling independent of the spurious amplitude-coupling introduced through signal orthogonalization (Hypothesis 1.1). Second, we assessed the relationship between genuine amplitude- and phase-coupling cortical networks for a broad range of frequencies (Hypothesis 1.2).

3.2 Materials and methods

3.2.1 Subjects and dataset

We analyzed resting-state MEG measurements from 95 subjects included in the publicly available human connectome project (HCP) S900 release. Participants were healthy adults in the age range between 22-35 ($n_{22\text{-}25}$=18, $n_{26\text{-}30}$=40, $n_{31\text{-}35}$=37), including 45 females. The resting-state measurements included up to three six-minute blocks with short breaks in between measurements. Data were recorded with a whole-head Magnes 3600 scanner (4D Neuroimaging, San Diego, CA, USA) situated in a magnetically shielded room (for further details see: Larson-Prior et al., 2013). Additionally, subjects were scanned on a Siemens 3T Skyra to acquire structural T1-weighted magnetic resonance images (MRI) with 0.7 mm isotropic resolution (Van Essen et al., 2013).

3.2.2 Data preprocessing

We used the preprocessed data as provided by the HCP pipeline (Larson-Prior et al., 2013). This includes removal of noisy and bad channels, bad data segments and physiological artifacts by the iterative application of temporal and spatial independent component analysis (ICA) (Larson-Prior et al., 2013; Mantini et al., 2011).

3.2.3 Physical forward model and source modeling

MEG sensors were aligned to the individual anatomy using FieldTrip (Oostenveld et al., 2010). We segmented the individual T1-weighted images and generated a single shell head model to compute the physical forward model (Nolte, 2003). We computed the forward model for 457 equally spaced (~1.2 cm distance) source points spanning the cortex at 0.7 cm depth below the pial surface (Hipp and Siegel, 2015). This source shell was generated in MNI-space and non-linearly transformed to individual headspace. Source coordinates, head model and MEG channels were co-registered on the basis of three head localization coils.

The sensor-level MEG data was projected to source space using linear beamforming (Gross et al., 2001; Van Veen et al., 1997). This spatial filtering approach reconstructs activity of the sources of interest with unit gain while maximally suppressing contributions from other sources.

Coordinates for the seed-based connectivity analyses were adopted from Hipp et al. (2012). For every seed, the source location of the 457 shell positions with minimum Euclidean distance from the seed coordinates was chosen: left auditory cortex (lAC) [-54, -22, 10]; left somatosensory cortex (lSSC) [42, -26, 54]; medial prefrontal cortex (MPFC) [-3, 39, -2] (all MNI coordinates).

3.2.4 Spectral analysis

Time-frequency estimates of the time-domain MEG signal were generated using Morlet's wavelets (Goupillaud et al., 1984). The bandwidth of the wavelets was set to 0.5 octaves (1 spectral standard deviation) with a temporal step-size of half the temporal standard deviation. We derived spectral estimates for frequencies from 1 to 128 Hz in quarter octave steps.

3.2.5 Coupling measures

We estimated amplitude-coupling using amplitude envelope correlations of orthogonalized signals (Hipp et al., 2012). Volume conduction effects were discounted by orthogonalizing the two complex signals at each point in time before correlation (Brookes et al., 2012; Hipp et al., 2012):

$$y_{orth}(t,f) = imag(y(t,f)\frac{x(t,f)'}{|x(t,f)|})$$

The $imag$ operator describes the imaginary part of the signal. The complex signals x and y are a function of time and frequency. x' is the complex conjugate of x. Discounting volume conduction with orthogonalization is only optimal for data with a Gaussian distribution (Brookes et al., 2014). Finally, we computed the Pearson correlation between the logarithm of power envelopes of the signals x and y_{orth}.

As a measure of phase-coupling we applied the weighted phase lag index (wPLI; Vinck et al., 2011). The wPLI takes only the imaginary part of the cross-spectrum into account and normalizes it with the average absolute imaginary contribution within the time series.

$$wPLI = \frac{|mean\left(imag\left(C_{x,y}\right)\right)|}{mean(|imag\left(C_{x,y}\right)|)}$$

$$C_{x,y} = xy'$$

Here, $C_{x,y}$ is the cross-spectrum between the two complex signals x and y defined as the product of x and the complex conjugate of y. The imaginary part of the cross-spectrum is insensitive to volume conduction since it has no contribution from zero phase lagged parts of the signal (Nolte et al., 2004; Vinck et al., 2011). We computed both coupling measures for the full correlation matrices for all subjects and frequency bands.

3.2.6 Data simulation

Palva and colleagues (2018) showed that amplitude correlations based on orthogonalized signals yield spurious correlations, given a consistent non-zero phase delay between signals. We employed the simulation approach put forward by Palva and colleagues (2018) as a generative model to estimate these spurious correlations. We computed a model for every connection, subject and frequency using empirical values for the free parameters. With this approach, we generated complete correlation matrices for every subject and frequency to estimate the spatial patterns of spurious amplitude-coupling. We modeled every two signals x and y

$$x = A_x(t)e^{ip_x(t)} + mA_y(t)e^{i(p_y(t)+s_{x,y})}$$

$$y = A_y(t)e^{i(p_y(t)+s_{x,y})} + mA_x(t)e^{ip_x(t)}$$

where $A(t)$ and $p(t)$ are vectors representing the amplitude and the phase of the sources, respectively. In analogy to volume conduction, the source data is linearly mixed by the parameter m. This value is determined from the empirical data as the multiplication of the filter matrix $F_{x,f}$ with the leadfield L_y (i.e, the resolution matrix) projected onto the first principal dipole direction $P1$ at x.

$$m(f)_{x,y} = F_{x,f}L_yP1_x$$

For every connection, we computed the model in both directions. $s_{x,y}$ is the phase shift between the two signals and was set to the estimated empirical phase shift for every connection, frequency and subject (see 2.7 below).

We determined the amplitude $A(t)$ vectors as follows:

$$A_x(t) = |F\big(n_1(t) + c_A n_2(t)\big)|$$

$$A_y(t) = |F\big(n_2(t) + c_A n_1(t)\big)|$$

where $n_1(t)$ and $n_2(t)$ are vectors of normally distributed random numbers with data length of 300 s, a pink spectrum and a sampling frequency of 400 Hz approximately matching the original data (Larson-Prior et al., 2013). The || operator refers to the modulus. c_A denotes the amplitude-coupling between the sources x and y, which was set to 0. The function F is the complex wavelet transformation of the vectors at the frequency of interest. The wavelet transformation parameters matched our analysis of the empirical data (see above). Analogously, we generated the phase $p(t)$ vectors:

$$p_x(t) = angle(F\left(n_3(t) + c_p n_4(t)\right))$$

$$p_y(t) = angle(F\left(n_4(t) + c_p n_3(t)\right))$$

where $n_3(t)$ and $n_4(t)$ are again 300 s vectors of normally distributed random numbers with a pink spectrum at a sampling frequency of 400 Hz. All 4 n-vectors were drawn anew for every connection and simulation run (see below). c_p denotes the phase-coupling and was set to the estimated empirical phase-coupling for every connection, frequency and subject (see 2.7 below).

Finally, we computed the amplitude-coupling of the orthogonalized signals x and y (see above) to quantify the strength of amplitude-coupling (AC_{spur}) that would be expected given the empirical parameters and no ground truth amplitude-coupling (c_a = 0). We computed the full correlation matrices for every subject and frequency. To reduce the variance induced by finite sampling, we averaged the correlation matrices across ten simulations. Furthermore, we averaged the two directions of orthogonalization, x on y and y on x, in the final correlation matrices. We correlated the spatial patterns P_{ACspur} of spurious amplitude-coupling with the spatial patterns of empirically measured amplitude-coupling P_{ACmeas} to quantify the similarity of these spatial patterns.

Finally, we orthogonalized the measured amplitude-coupling patterns to the spurious amplitude-coupling patterns by linear regression to estimate the corrected amplitude-coupling patterns.

3.2.7 Estimated empirical phase shift and phase-coupling

The wPLI quantifies phase-coupling but is not identical to the phase-coupling c_p employed in the above simulations. In other words, if one simulates two signals with c_p set to an empirically measured wPLI the simulated signals will have a wPLI that is different from the empirically measured wPLI. The same applies to the phase shift $s_{x,y}$ between the two signals. The empirical statistics and their model parameters show a monotonous interaction but are not numerically identical. Thus, for each connection, frequency and subject, we employed a grid search approach to estimate the parameter setup (c_p and $s_{x,y}$) under which the simulated signals had the least deviation from the empirically measured wPLI and phase shift.

For the grid search we simulated signals as described above (see 2.6) 800,000 times covering the entire space of possible mixings, phase-couplings and phase shifts: mixing m between 0 to 1 (in steps of 0.01), phase shift $s_{x,y}$ between 0 and π (in steps of π/100) and phase-coupling c_p between 0 and 0.8 (in steps of 0.01). For each parameter combination, we computed the phase shift, i.e. the angle of the mean complex coherency, and the wPLI of the simulated signals. To stabilize these estimates, we averaged these values across 1000 repetitions within each combination. For any connection with a given mixing m, we determined which combination of c_p and $s_{x,y}$ yielded the empirically measured wPLI and phase shift of the simulated signal. We then employed this estimated parameters for each simulated connection in the main experiment (see Fig. A1 for an example and assessment of the estimation quality).

3.2.8 Reliability estimation

To compare the reliability, i.e. reproducibility, of functional connectivity measures, we correlated the seed-based connectivity patterns. We first averaged the correlation matrices acquired in the three runs of each subject before performing pairwise correlations between subjects (between-subjects reliability, rel_{bs}).

$$rel_{bs,M1,M2,s1,s2,f} = corr(P_{M1,s1,f}, P_{M2,s2,f})$$

where $M1\ and\ M2$ denote the different connectivity measures (AC_{spur}, AC_{meas}, or PC). A pattern P describes the connectivity of a given seed with the rest of the source-model, i.e. one column of the full correlation matrix. $\mathrm{s1\ and\ s2}$ denote the subjects involved in the

computation, where $s1 \neq s2$. All reliabilities were independently computed as a function of frequency f.

Only reliable signals can be correlated and corrected for attenuation (see below). Therefore, we statistically tested for reliabilities larger than zero (one-sided t-test, df = 94 (n = 95), FDR correction, see below) and excluded connections with non-significant reliability. We found that 99%, 95% and 95% of the connections spanning all frequencies were reliable for measured amplitude-coupling, spurious amplitude-coupling and phase-coupling, respectively.

3.2.9 Pattern similarity, inter-measure correlation and attenuation correction

We correlated the correlation patterns between different metrics, i.e. AC_{spur} vs. AC_{meas}, AC_{spur} vs. PC, AC_{meas} vs. PC:

$$ic_{ACspur,ACmeas,i,s1,s2,f} = corr(P_{ACspur,i,s1,f}, P_{ACmeas,i,s2,f})$$

$$ic_{ACspur,PC,i,s1,s2,f} = corr\left(P_{ACspur,i,s1,f}, P_{PC,i,s2,f}\right)$$

$$ic_{PC,ACmeas,i,s1,s2,f} = corr(P_{PC,i,s1,f}, P_{ACmeas,i,s2,f})$$

The inter-measure correlation ic between two metrics is defined as the Pearson correlation ($corr$) of the seed-based connectivity patterns P at seed i and frequency f computed between different subjects $s1 \neq s2$. The seed pattern P is defined as the connectivity of a given seed with the remaining 456 source points, i.e. one column in the full correlation matrix. We computed the inter-measure correlations ic for all 8930 unique subject pairings (95^2-95), 457 connectivity patterns, 3 metric combinations, and 29 frequencies.

The measured inter-measure correlations do not only reflect the true underlying similarity of patterns but also the reliability with which these patterns are estimated. Measured correlation decreases with decreasing pattern reliability even if the true underlying pattern correlation remains identical (Fig. 1, dashed lines). This effect of reliability is known as attenuated correlations (Spearman, 1904). Following Spearman (1904), we corrected for this attenuation and normalized the mean inter-measure correlation $ic_{M1,M2}$ by the pooled reliabilities within the measures rel_{M1} and rel_{M2}.

$$\overline{ic}_{M1,M2,i,f} = Z^{-1}(mean_s\left(Z\left(ic_{M1,M2,i,s1,s2,f}\right)\right))$$

$$\overline{rel}_{M1,i,f} = Z^{-1}(mean_s\left(Z\left(rel_{bs,M1,s1,s2,f}\right)\right))$$

$$\overline{rel}_{M2,i,f} = Z^{-1}(mean_s\left(Z\left(rel_{bs,M2,s1,s2,f}\right)\right))$$

where the mean inter-measure correlation ic for different metric combinations $M1/M2$ is defined as the mean over all possible subject combinations s with $s1 \neq s2$. The same averaging is done for the reliabilities within the measures $M1$ and $M2$. The function Z denotes the Fisher Z-transformation and Z^{-1} the inverse transformation:

$$Fisher's\ Z = \frac{1}{2}\ln\left(\frac{1+r}{1-r}\right) = \text{artanh}\ (r)$$

$$Fisher's\ Z^{-1} = r = \frac{e^{2Z}-1}{e^{2Z}+1} = \tanh\ (Z)$$

Here, ln denotes the natural logarithm, $artanh$ the inverse hyperbolic tangent, $tanh$ the tangent function, e Euler's number and r is the correlation coefficient. Finally, the attenuation corrected inter-measure correlation icc is defined as:

$$icc_{M1,M2,i,f} = \frac{\overline{ic}_{M1,M2,i,f}}{\sqrt{\overline{rel}_{M1,i,f}}\sqrt{\overline{rel}_{M2,i,f}}}$$

3.2.10 Simulation of attenuation corrected correlations

The attenuation corrected inter-measure correlation is unbiased. Accordingly, independent of the reliability with which two patterns are measured, their expected attenuation corrected correlation is the true underlying correlation of these patterns. This is well illustrated by simulations (Fig. 1). We simulated two connectivity patterns of size N (n=45, approximating the effective degrees of freedom of the source-level MEG data; Hipp and Siegel, 2015) by drawing two times N data points from a normal distribution and applying the inverse Fisher's Z transformation. The resulting Nx2 matrix with both patterns is defined as P. From P we then computed $\mathrm{P_r}$ with a predefined correlation r between the two patterns. To this end, we defined the desired full correlation matrix R between the two patters as:

$$R = \begin{bmatrix} 1 & r \\ r & 1 \end{bmatrix}$$

Then, we applied the Cholesky factorization $chol$ of R and multiplied P by the resulting matrix:

$$P_r = P * chol(R_r)$$

We simulated two cases, r=1 and r=0.3. Due to finite sampling the resulting correlation of the two vectors in $\mathrm{P_r}$ only approximates r. We therefore only used patterns for which the measured correlation coefficient differed from r by maximally 0.05. This threshold is necessary to not conflate the spread of the attenuation-corrected correlation distributions with the variance of the simulated vector correlation, which otherwise grows towards $\mathrm{r} = 0$. We replicated the patterns for n=95 subjects and added inverse Fisher's Z-transformed normally distributed noise independently to every subject's $\mathrm{P_r}$ with varying signal-to noise ratios of 0.5, 1, 2. Then, we computed the inter-measure correlation between patterns and the attenuation corrected correlation patterns and repeated the simulation 10,000 times for every SNR. The results are shown in Fig. 1.

3.2.11 Statistical testing of attenuation corrected correlations

A perfect attenuation corrected correlation ($icc = 1$) indicates that two cortical patterns are identical if there was perfect reliability. A value smaller than 1 indicates that there is a difference between the two patterns that cannot be explained by reduced reliability. Similarly, a value different from 0 indicates pattern similarity. For statistical testing of icc, we applied leave-one-out Jackknifing and computed icc pseudo-values for each subject, source and frequency. We tested the generated pseudo-value distributions for normality using the Kolmogorov-Smirnov test. We then performed one-sided t-tests against 1 when appropriate. We corrected the resulting p-values with false-discovery rate correction across frequencies (Benjamini and Hochberg, 1995).

Notably, statistical testing re-introduces the reliability confound discussed above. While the mean pseudo-values of attenuation corrected correlations are independent of reliability, their variability across subjects increases with decreasing reliability (see also Fig. 1). This confound needs to be taken into account when interpreting the statistical significance.

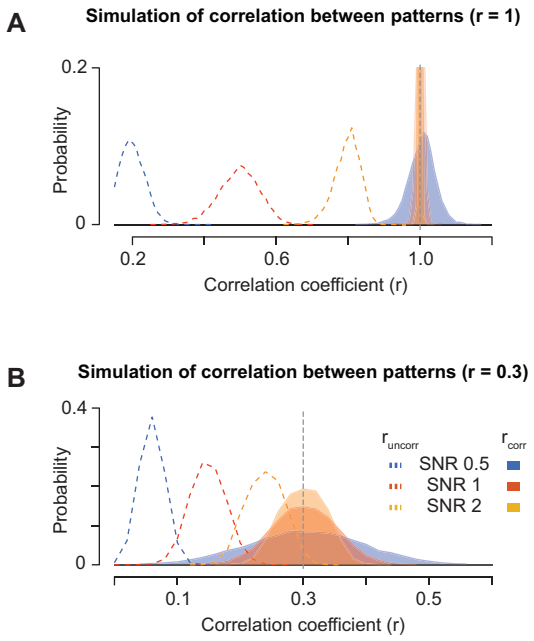

Figure 1. Simulation of attenuation corrected and uncorrected pattern correlation as a function of ground-truth pattern correlation and between-subject noise

Distribution of simulated attenuation corrected (solid lines) and uncorrected correlations (dashed lines) between perfectly correlated patterns (**A**) and patterns correlated at r=0.3 (**B**). We added uncorrelated noise to the patterns: The signal-to-noise ratio (SNR) levels are set to 0.5, 1 and 2 (for further details see 2.10). The y-axis in (A) is trimmed to 0.2 for visualization purposes: maximum values for SNR 1=0.4 and SNR 2=0.83.

3.3 Results

We quantified brain-wide neuronal phase- and amplitude-coupling from resting-state MEG measurements in 95 healthy participants. We applied source-reconstruction (Van Veen et al., 1997) to systematically characterize neuronal coupling at the cortical source level. Field spread (or signal leakage) can induce spurious coupling of sensor- and source-level M/EEG signals. Thus, we employed two coupling measures discounting signal leakage. We quantified phase-coupling using the weighted phase lag index (wPLI; Nolte et al., 2004; Vinck et al., 2011), which shows the best reliability of phase-coupling measures free from volume-conduction (Colclough et al., 2016). Further, for the presented data wPLI showed the same coupling patterns as the imaginary coherence or the phase lag index (see Fig. A2 for a comparison of the wPLI with these other phase-coupling measures). For amplitude-coupling, we employed pair-wise signal

orthogonalization before estimating amplitude envelope-correlations (Fig. 2A) (Brookes et al., 2012; Hipp et al., 2012).

It has recently been shown that signal orthogonalization does not perfectly discount volume conduction in the presence of genuine phase-coupling with non-zero phase delays (Palva et al., 2018). Intuitively, this is because in the presence of signal leakage, such phase-coupling systematically rotates the estimate of the signal to which one aims to orthogonalize, which results in sub-optimal orthogonalization and spurious amplitude-correlations (Fig. 2B). Thus, our first question was if the empirically measured amplitude-coupling patterns solely reflect this spurious amplitude-coupling. To test this, we directly estimated the spurious amplitude-coupling with numerical simulations based on empirical parameters (see 2.6). In brief, for each subject, connection, and frequency, we simulated pairs of cortical signals with their signal leakage (resolution matrix), measured phase-coupling (wPLI) and measured mean phase shift, but with no amplitude-coupling. We then estimated the spuriously measured amplitude-coupling for such signals. With this approach we computed the cortex-wide patterns of spurious amplitude-coupling to be expected under the assumption of no genuine amplitude-coupling.

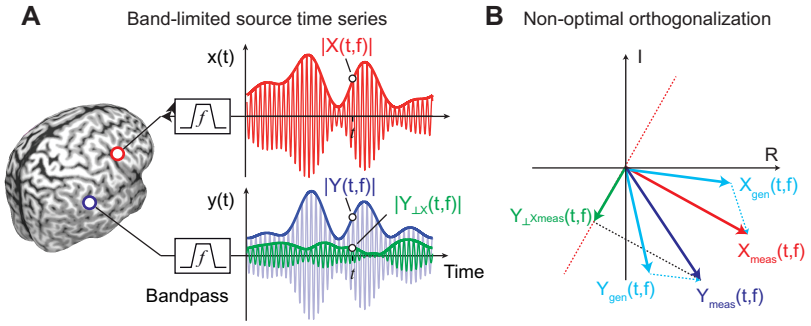

Figure 2. Principle of signal leakage reduction for amplitude relations

(**A**) Illustration of band-limited time series from two sources X (red, upper panel) and Y (blue, middle panel) with their envelopes (thick lines). The green thick line represents the envelope of signal Y orthogonalized on signal X. (**B**) illustrates how the orthogonalization can induce spurious amplitude-coupling in the presence of phase-coupling and signal leakage. Here, we orthogonalize the measured signal Y_{meas} onto the measured signal X_{meas}. In the presence of signal leakage, both measured signals reflect a mix of the genuine signals X_{gen} and Y_{gen}. For non-zero phase-coupling between X_{gen} and Y_{gen}, X_{meas} is rotated away from X_{gen}. This causes sub-optimal signal orthogonalization and spurious amplitude-coupling.

3.3.1 Seed-Based Connectivity Analysis

We started with a seed-based analysis (Fig. 3). We computed cortex-wide patterns of measured (Fig. 3A) and spurious (Fig. 3B) amplitude-coupling as well as phase-coupling (Fig. 3C) at 16 Hz for several early sensory and higher-order cortical regions. As early sensory regions we chose the primary auditory (A1) and the somatosensory cortex (S1), which show strong inter-hemispheric connectivity and robust amplitude-coupling patterns at 16 Hz (Hipp et al., 2012; Mehrkanoon et al., 2014; Siems et al., 2016). For each seed, subject and both coupling modes, we z-scored the raw coupling measures and tested for z-scores larger than zero across subjects (one-sided t-test, FDR-corrected). This revealed which connections showed significant above-average coupling, discounting global offsets of coupling measures (Hipp et al., 2012).

For both sensory seeds (A1 and S1), amplitude-coupling was strongest to regions surrounding the seed region and to the homologous area in the other hemisphere (Fig. 3A). Phase-coupling did not show this pattern, but only above-average connectivity surrounding the seed (Fig. 3C). Similarly, spurious amplitude-coupling was restricted to regions surrounding the seed (Fig. 3B).

Our findings for a higher-order seed region confirmed these results. We investigated phase- and amplitude-coupling for the medial prefrontal cortex (MPFC, Fig. 3A-C bottom row), which shows a complex connectivity structure for amplitude-coupling at 16 Hz (Hipp et al., 2012; Siems et al., 2016). We found that amplitude-coupling of MPFC peaked bilaterally in the dorsal prefrontal and lateral parietal cortices. In contrast, phase-coupling and spurious amplitude-coupling only peaked surrounding the seed region.

We extended our analysis to the entire correlation matrix at 16 Hz (Fig. 3D). The results confirm the observations from the seed-based analyses. In comparison to phase-coupling and spurious amplitude-coupling, measured amplitude-coupling displayed the most pronounced interhemispheric connectivity.

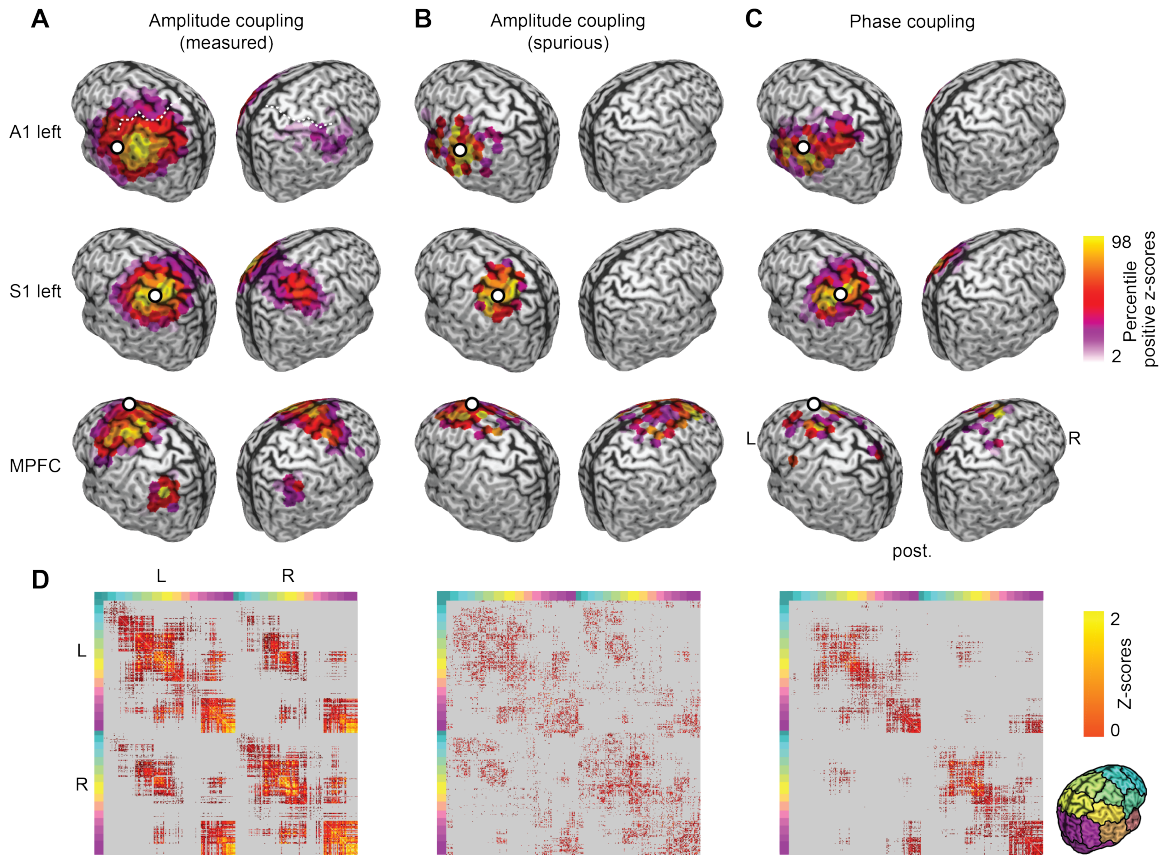

Figure 3. Seed based analysis for early sensory and higher order cortices at 16Hz

Seed-based correlation structure (z-scores) of the left auditory (left A1, top row), left somatosensory (left S1, middle row), and the medial prefrontal cortex (MPFC, bottom row) for measured amplitude-coupling (**A**), spurious amplitude-coupling due to phase-coupling (**B**) and measured phase-coupling (**C**). Coupling z-scores are tested against zero and statistically masked ($p<0.05$, FDR corrected). Color scale ranges from the 2^{nd} to the 98^{th} percentile of significant values, scaled within each panel. White dots indicate seed regions. The white dashed line in the top left panel highlights the central sulcus (see 4.3 for exact seed coordinates). (**D**) Full cortico-cortical connectivity at 16Hz. Seed-wise coupling z-scores are tested against zero and statistically masked ($p<0.05$, FDR corrected). Gray areas indicate non-significant connections. Colored marginals and the inset on the bottom right indicate the ordering of cortical seeds.

3.3.2 Genuine amplitude-coupling

To quantitatively address our first main question, i.e. if the measured amplitude-coupling reflects genuine amplitude-coupling, we systematically assessed the similarity of the cortical patterns of spurious and measured amplitude-coupling across frequencies (Fig. 4).

For each frequency and both measures, we computed the coupling between all cortical regions, i.e. we computed the full connectivity matrices of the cortex-wide measured and spurious amplitude-coupling (as shown in Fig 3D for 16 Hz). We then correlated the patterns of spurious and measured amplitude-coupling for each cortical seed region (3 examples from all 457 sources at one frequency are shown in Fig. 3). In other words, we correlated each column of the connectivity matrices between measures. Averaged across all seed regions and all frequencies, this revealed a very low correlation between spurious and measured amplitude-coupling patterns with median correlation coefficients below 0.05 (Fig. 4A, yellow line).

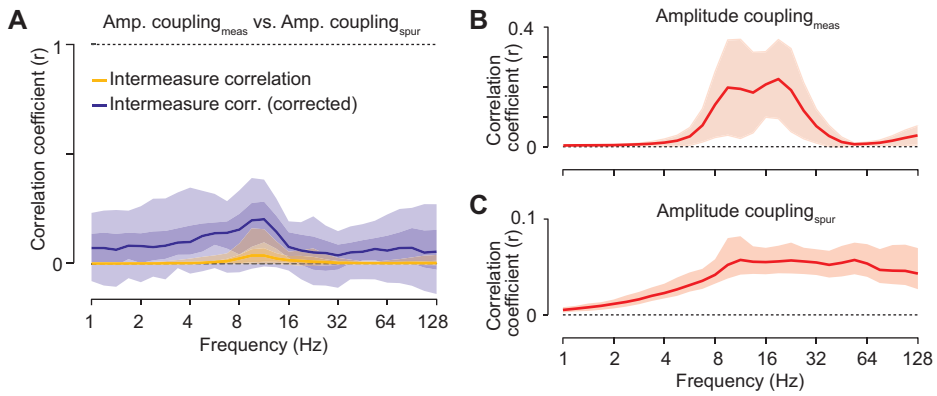

Figure 4. Correlation between measured and spurious amplitude-coupling patterns
(**A**) Frequency resolved correlation between measured and spurious amplitude-coupling patterns. Lines indicate median attenuation corrected (blue) and uncorrected (yellow) correlation. Shaded areas indicate the 5-95% and 25-75% inter-percentile range across cortical space. (**B**) Reliability, i.e. correlation, of measured amplitude-coupling patterns between subjects. (**C**) Reliability of spurious amplitude-coupling patterns between subjects. Shaded areas indicate the 5-95% interquantile range.

At first sight, the low correlation between measured and spurious amplitude-coupling patterns suggests that there is indeed genuine amplitude-coupling. However, it is important to realize that the correlation between two metrics does not only reflect their true underlying correlation, but also the metrics' reliability (Bergholm et al., 2010; Hipp et al., 2012; Siems et al., 2016; Spearman, 1904). A reduced reliability of two measures, e.g. due to noise, leads to a lower measured correlation even if the true underlying correlation between the two measures is higher (Fig. 1, dashed lines). Thus, the observed low and frequency-specific correlation between spurious and measured amplitude-coupling patterns may merely reflect the low reliability of either measure (Fig. 4B & C), and thus, does not allow for directly inferring genuine amplitude-coupling.

We applied attenuation correction of correlations (Hipp and Siegel, 2015; Siems et al., 2016; Spearman, 1904) to account for the effect of signal reliability. Attenuation corrected correlations quantify how strong a correlation would be for perfectly reliable signals (Fig. 1). We employed the between-subject correlation of the measured and spurious amplitude-coupling patterns as a proxy for each measure's reliability. For the measured amplitude-coupling, between-subject reliability peaked around 16 Hz (Fig. 4B) which is compatible with previous findings (Hipp and Siegel, 2015; Siems et al., 2016). For the spurious amplitude-coupling, reliability was overall lower and decreased for frequencies below 16 Hz (Fig. 4C).

We corrected the correlation between measured and spurious amplitude-coupling patterns for these reliabilities by pooled division (Fig. 4A, blue line). As predicted, the overall correlation between measured and spurious amplitude-coupling patterns increased. However, the median attenuation corrected correlation remained low between 0.05 and 0.19 for all frequencies. We statistically assessed if there was indeed spurious amplitude-coupling contributing to the measured amplitude-coupling, i.e. if the attenuation corrected correlations between measured and spurious amplitude-coupling patterns were significantly different from 0. Attenuation corrected correlation is an unbiased estimate (Fig. 1). Thus, we applied a leave-one-out jackknifing procedure and false-discovery rate correction (Benjamini and Hochberg, 1995). Across the entire spectrum, we found that less than 1% of the seed patterns showed significant ($p<0.05$, FDR-corrected) correlations with spurious amplitude-coupling patterns. On average, across all frequencies and cortical seeds, less than 2% of the variance in the measured amplitude-coupling patterns could be explained by spurious amplitude-coupling.

The above simulations may not capture all non-linearities in the relationship of phase-coupling, amplitude-coupling and spurious amplitude-coupling. Thus, we repeated our analysis using a non-parametric rank correlation that is insensitive to monotonous non-linearities (Fig. A3). The results of this control analysis were nearly identical to the results based on Pearson's correlation. Taken together, we concluded that, for the data at hand, the effect of spurious amplitude-coupling on measured amplitude-coupling patterns was small.

Why does the spurious amplitude show little effect on the measured amplitude-coupling? We speculated that this might be due to the dynamic range of empirical phase-coupling. To investigate this, we performed systematic simulations across a broad set of coupling parameters and mixing (compare Palva et al., 2018) (Fig. 5A). These simulations showed that only for substantial phase-coupling (c_p>=0.2) the relation between phase-shift, phase-coupling, mixing and spurious amplitude-coupling appears stable (Fig. 5A). However, the estimated empirical phase-coupling was mostly below this range (Fig. 5B). The median over all frequencies was between 0.01 and 0.09. For all frequencies but the lowest two, phase-coupling was below 0.2 and 0.3 for more than 95% and 99% of the connections, respectively (Fig. 5B). Complementarily, spurious amplitude-coupling values approached the levels of measured amplitude-coupling (Fig. 5C) only at higher phase-coupling (c_p>=0.4) at a phase shift of around 90 degrees (Fig. 5A). Thus, for the present data, the observed small effect of spurious amplitude-coupling on the measured amplitude-coupling is likely due to the small empirical phase-coupling.

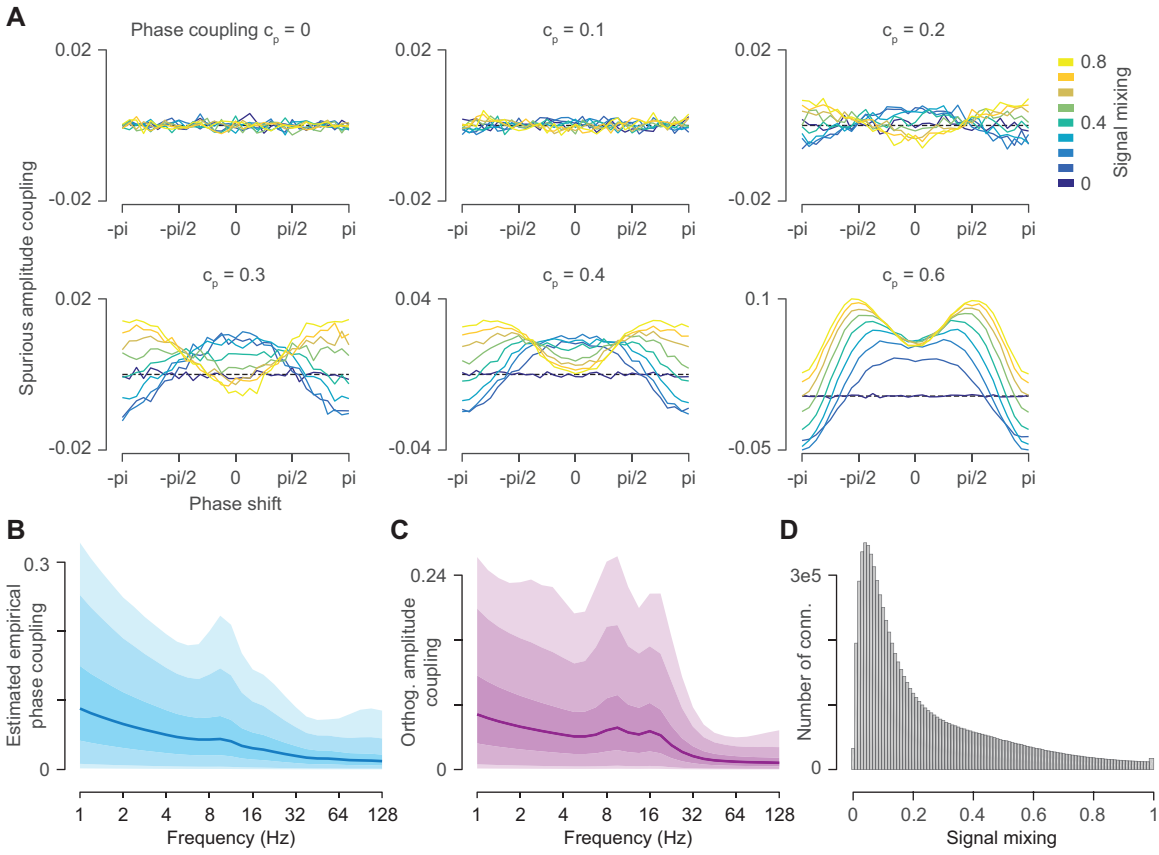

Figure 5. Systematic simulation of spurious amplitude-coupling and empirical parameters (**A**) Simulation of spurious amplitude-coupling as function of phase-coupling (panels), phase shift between signals (-pi to pi) and signal mixing (colored lines). (**B**) Distribution of the estimated empirical phase-coupling (**C**) Distribution of the measured amplitude-coupling (**D**) Distribution of empirical signal mixing. All shaded areas indicate the 1-99%, 5-95% and 25-75% interquantile ranges.

3.3.3 Comparing amplitude-coupling and phase-coupling networks

The above results suggest that the measured amplitude-coupling patterns are dominated by genuine amplitude-coupling. This allowed us to address our second main question: Are amplitude- and phase-coupling patterns of cortical connectivity different?

To address this question, we partialized out the spurious amplitude-coupling patterns from the measured amplitude-coupling patterns using linear regression (see Fig. 6 for example seed patterns). We then correlated the resulting corrected amplitude-coupling patterns with the measured phase-coupling patterns for every seed pattern and

frequency. We found highest correlations from 8–26 Hz (Fig. 7A, yellow line). As for the correlation between spurious and measured amplitude-coupling patterns above, these correlations are attenuated by measurement reliability (Fig. 1 and 7B). We therefore computed the attenuation corrected correlation between the corrected amplitude-coupling and phase-coupling patterns.

The attenuation correction substantially increased the correlation, i.e. similarity between the two coupling modes (Fig. 7A, blue line). The median corrected correlation was around 0.8. The spectral distribution indicated three regimes: Very high similarity for frequencies below 4 Hz, a lower similarity from 5–64 Hz and very high variability of similarity above 64 Hz. We statistically tested if the two coupling modes shared pattern similarities, i.e. if the correlation was significantly different from 0. Indeed, for the entire spectrum and almost all seed patterns there was significant similarity between amplitude- and phase-coupling patterns (Fig. 7C, green line; $p<0.05$, corrected). However, even though the similarity was high, we found that the patterns were not identical. For almost all seed patterns at frequencies above 4 Hz pattern similarity was significantly smaller than 1 (Fig. 7C red line; $p<0.05$, corrected). Thus, amplitude- and phase-coupling patterns were similar but not identical. Again, we repeated the correlation analysis based on rank-correlation (Fig. A4). This yielded almost identical results suggesting that the dissimilarities were not driven by monotonous non-linear interactions between amplitude- and phase-coupling.

The average attenuation corrected correlations did not show strong spectral differences (Fig. 7A). However, the cortical distribution of connectivity patterns that are most dissimilar between coupling modes may be frequency specific. Indeed, for all investigated frequencies, we found cortical regions with significantly dissimilar amplitude- and phase-coupling patterns (Fig. 7C) and less than 25% shared variance between coupling patterns (Fig. 8). The median pattern across all frequencies (Fig. 8, bottom right) displayed the strongest differences bilaterally in lateral prefrontal, orbitofrontal, anterior temporal and temporo-parietal areas. The lateral prefrontal differences appear to be strongest in the theta to alpha frequency range (6–11 Hz) and the temporal differences in the beta (23 Hz) and low gamma (45 Hz) frequency ranges (Fig. 8).

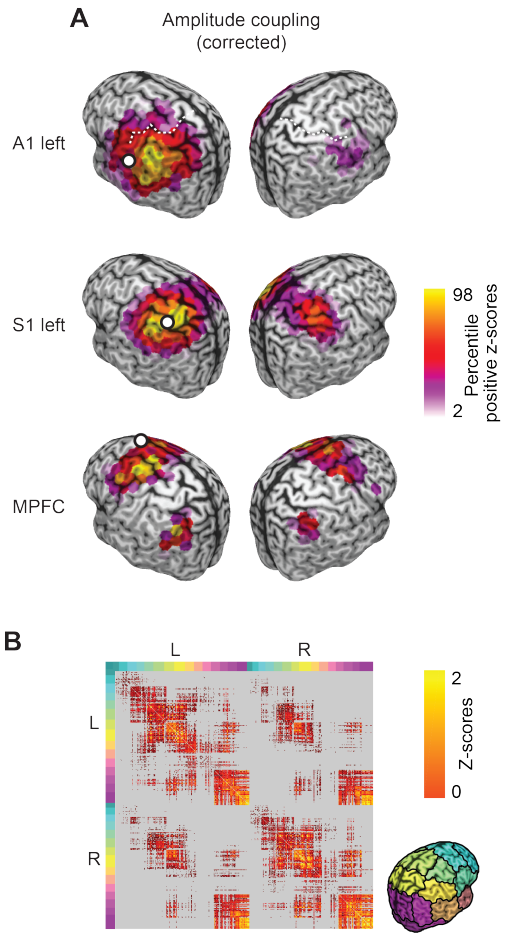

Figure 6. Corrected genuine amplitude-coupling patterns

(**A**) Seed-based correlation structure (z-scores) of the left auditory (left A1, top row), left somatosensory (left S1, middle row), and the medial prefrontal cortex (MPFC, bottom row) for the corrected amplitude-coupling at 16 Hz. Coupling z-scores are tested against zero and statistically masked ($p<0.05$, FDR corrected). Color scale ranges from the 2^{nd} to the 98^{th} percentile of significant values, scaled within each panel. White dots indicate seed regions. The white dashed line in the top left panel highlights the central sulcus (see Section 4.3 for exact seed coordinates). (**B**) Full cortico-cortical connectivity at 16 Hz. Seed-wise coupling z-scores were tested against zero and statistically masked ($p<0.05$, FDR corrected). Gray areas indicate non-significant connections. Colored marginals and the inset on the bottom right indicate the ordering of cortical seeds.

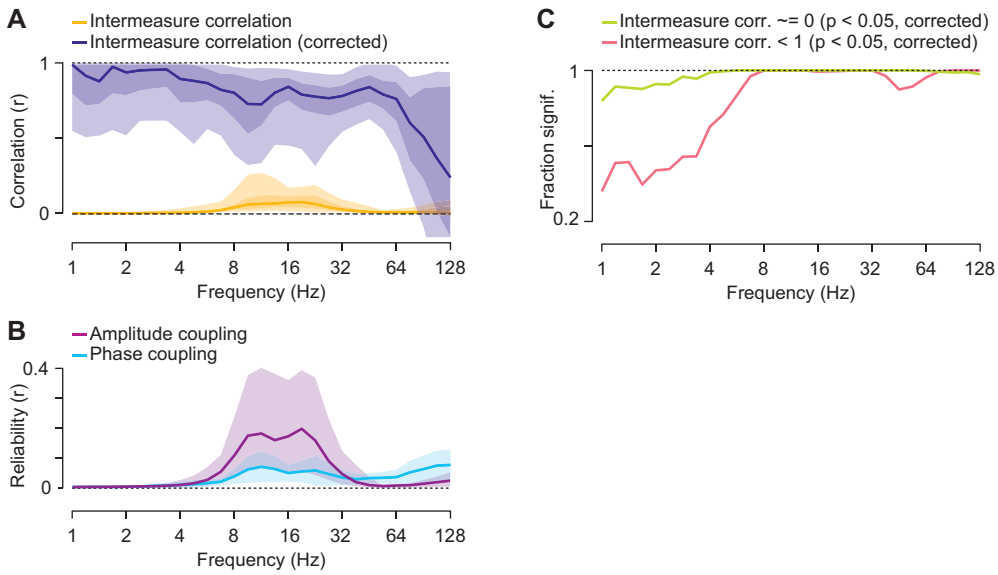

Figure 7. Correlation between amplitude- and phase-coupling patterns

(**A**) Spectrally resolved distribution of the correlation between corrected amplitude- and phase-coupling patterns. The lines show the median of the uncorrected (yellow) and attenuation corrected (blue) correlations. The shaded areas indicate the 5-95% and 25-75% interquantile range across cortical space. (**B**) Between-subject reliability of corrected amplitude-coupling (purple) and phase-coupling (cyan) as a function of frequency. Shaded areas indicate the 5-95% interquantile range across cortical space. (**C**) Spectrally resolved fraction of patterns that show an attenuation-corrected correlation significantly different from 0 (green line) or smaller than 1 (red line) ($p < 0.05$, FDR-corrected).

Which features of connectivity drive these differences between coupling modes? Given the higher complexity of amplitude-coupling patterns as compared to phase-coupling patterns (Fig. 3A & Fig. 6A), we investigated the relation between amplitude- and phase-coupling patterns as a function of spatial distance. We split all cortico-cortical connections into 4 quartiles and, for each quartile, repeated the correlation of connectivity patterns (Fig. 9). We found that patterns were most similar for short distance connections and were more dissociated for longer connections (Fig. 9B). Thus, the differences between amplitude- and phase-coupling patterns were mostly driven by differences of long-distance connectivity.

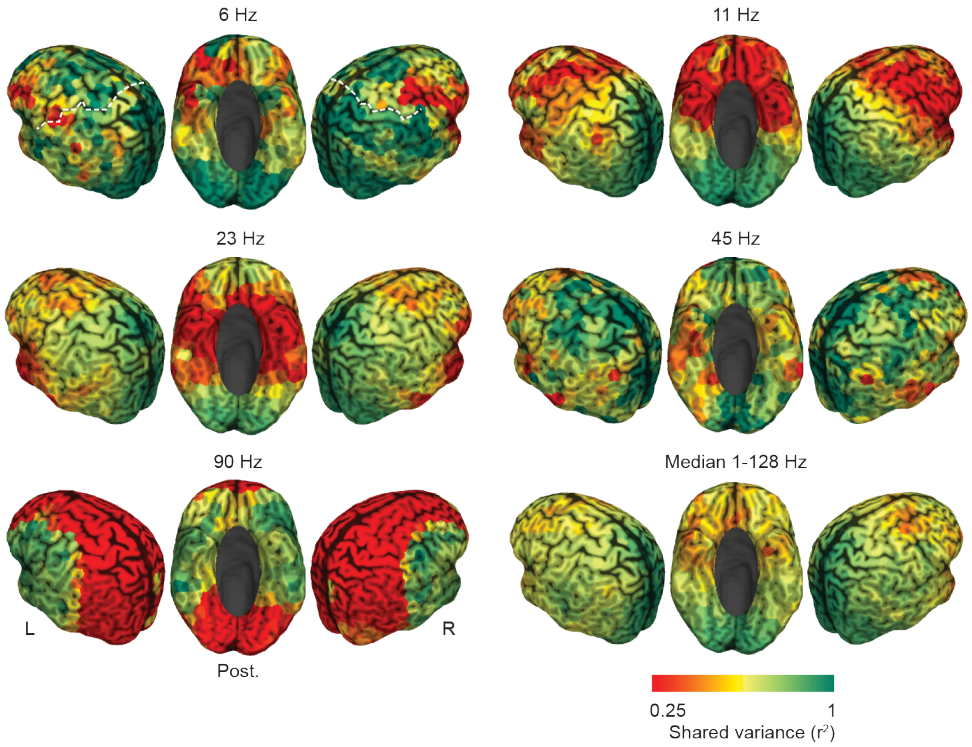

Figure 8. Cortical distribution of the correlation between amplitude- and phase-coupling patterns

Cortical distribution of the shared variance (r^2) between corrected amplitude- and phase-coupling patterns for 6 Hz, 11 Hz, 23 Hz, 45 Hz and 90 Hz. The bottom right panel shows the median across all assessed frequencies (1–128Hz). Red areas indicate differences whereas green areas indicate similarity between coupling modes. The white dashed line (top left panel) indicates the central sulcus.

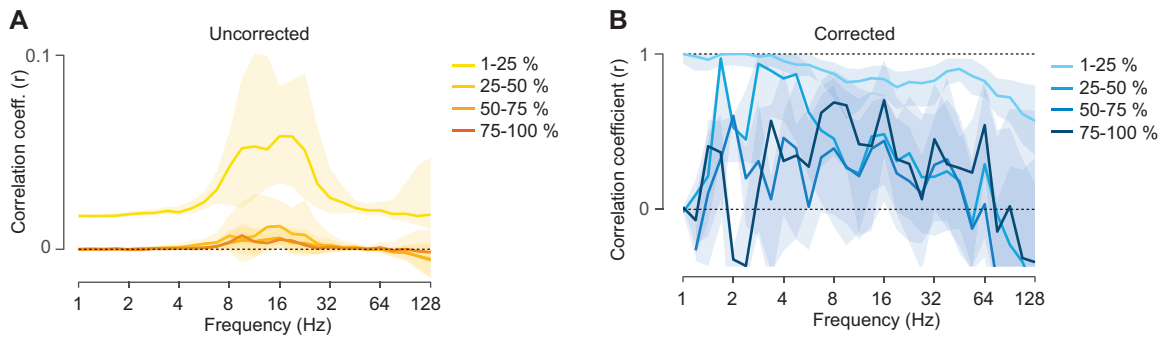

Figure 9. Correlation between amplitude- and phase-coupling patterns as a function of connection distance

Spectrally resolved correlation between corrected amplitude- and phase-coupling patterns for different quartiles of Euclidean distance between the cortical seeds of each connection. (**A**) Uncorrected and (**B**) attenuation corrected correlation between corrected amplitude-coupling and phase-coupling patterns. Shaded areas indicate the 25-75% interquartile range over space.

3.4 Discussion

Our results provide, to our knowledge, the first systematic comparison of cortical phase- and amplitude-coupling patterns in the human brain. We found similarities and differences between both coupling modes that were widely distributed across frequencies and the entire cortex (Hypothesis 1.2). By combining empirical measurements and simulations we showed that the observed differences were not caused by known methodological biases, but instead reflect a genuine dissociation between coupling modes (Hypothesis 1.1). The observed differences suggest that the two coupling modes may at least partly reflect distinct neural mechanisms. Furthermore, our results highlight and clarify the compound nature of amplitude-coupling measures applied to orthogonalized signals.

3.4.1 Discounting confounding factors

Our analyses discount three critical factors that confound the estimation of neuronal coupling patterns and their comparison. First, we employed amplitude correlations of orthogonalized signals (Brookes et al., 2012; Hipp et al., 2012) and the weighted phase-lag index (Vinck et al., 2011). Using these coupling measures ensured that the measured coupling did not reflect spurious coupling due to field-spread.

Second, recent studies suggest that amplitude correlation between orthogonalized signals is a compound measure, which is affected by the phase-coupling between those signals (Palva et al., 2018). We estimated the spurious amplitude-coupling due to phase-coupling using simulations based on the empirically measured phase-coupling. We then partialized the resulting spurious amplitude-coupling patterns from the measured amplitude-coupling patterns.

Third, for the comparison between coupling modes, we employed attenuation correction of correlations (Spearman, 1904). This approach allows correcting for the attenuation of measured correlation caused by sub-optimal measurement reliability. Attenuation correction of correlations is a powerful analytical approach that has been successfully employed before to compare MEG with fMRI (Hipp and Siegel, 2015) and MEG with EEG (Siems et al., 2016). Importantly, reliability in the present study refers to the stability of coupling patterns across subjects, which effectively takes into account all sources of variance across subjects, including measurement and finite-sampling noise, noise caused by neural activity not of interest, and inter-subject variability. The employed approach corrects for all these sources of variance, which attenuate measured correlations and may thus induce spurious spectral and spatial specificity.

Our results indicate that the raw correlation between amplitude- and phase-coupling patterns is strongly affected by measurement reliability. Attenuation correction suggests that the raw correlation peak around 16 Hz reflects the strength of intrinsic cortical rhythms around this frequency, rather than a frequency-specific relation of the two coupling modes (compare also Zhigalov et al., 2017).

3.4.2 Phase-coupling sensitivity of orthogonalized amplitude correlation

Our results provide a critical reassessment of well-established amplitude-coupling measures of orthogonalized signals (Brookes et al., 2012; Hipp et al., 2012). It has recently been pointed out that, in the presence of field-spread, these measures are sensitive to phase-coupling with non-zero phase lag (Palva et al., 2018). Here, we combined the simulation approach put forward by Palva and colleagues (2018) with empirical measurements to systematically evaluate the sensitivity of these measures to phase-coupling across the human cortex.

The bias of orthogonalized amplitude-coupling measures left open the possibility that the described amplitude-coupling patterns (Brookes et al., 2012; Hipp et al., 2012) merely reflect phase-coupling in combination with field spread. Our results provide several lines of evidence against this hypothesis.

First, the spurious amplitude correlation showed little consistent connectivity, whereas the measured amplitude-coupling patterns showed complex and multimodal distributions (Fig. 3). Second, the between-subject reliability of coupling patterns clearly dissociated measured and spurious amplitude-coupling (Fig. 4B and C). Third, for all frequencies and cortical regions spurious amplitude-coupling patterns could not explain more than 10% and on average less than 4% of the variance in measured amplitude-coupling patterns (Fig. 4A). In sum, our findings suggest that for the present data the magnitude of spurious amplitude-coupling and its effects on measured amplitude-coupling is small.

Nevertheless, it is important to highlight the compound nature of amplitude correlations of orthogonalized signals. Our simulations confirm that phase-coupling, phase shift and mixing have a marked effect on the amount of spurious amplitude-coupling (Fig. 5A). In accordance with Palva and colleagues (2018), our results show that this compound nature needs to be taken into account in particular for cases with high or variable phase-coupling.

3.4.3 Relation between phase- and amplitude-coupling

Our results show that amplitude- and phase-coupling patterns bear substantial similarities (Fig. 7). These similarities may result from one or more common underlying neural mechanisms. Synaptic interactions between neuronal populations may induce both, coupling of phases and amplitudes of these neuronal populations. Similarly, common input to neuronal populations will co-modulate and thus couple both, phases and amplitudes (Tewarie et al., 2018a).

Alternatively, also causal relations between both coupling modes may result in correlations. For example, phase-locking may enhance neuronal interactions, and thereby, enhance amplitude-coupling (Fries, 2015; Womelsdorf et al., 2007).

Despite the high attenuation corrected correlation between amplitude- and phase-coupling patterns we found that amplitude- and phase-coupling patterns are not

identical. Which factors may cause the observed differences between phase- and amplitude-coupling patterns (Fig. 7)?

First, different non-linearities between coupling modes may induce differences. The same underlying neuronal interaction or common input may have different effects on both coupling modes. However, in contrast to our present results, this effect should be spectrally and spatially unspecific. Furthermore, our present results were robust to using a non-parametric correlation insensitive to monotonous non-linearities (Fig. 6). These results suggest that such non-linearities cannot fully explain the observed differences between coupling modes.

Second, distinct neuronal mechanisms may underlie the two coupling modes. On the one hand, for example, neuromodulation may co-modulate the amplitude of rhythms in different brain regions (van den Brink et al., 2019). Or, as recently proposed, slow fluctuations of extracellular potassium concentrations and structural connectivity may drive long-range power co-fluctuations (Krishnan et al., 2018). These mechanisms may induce amplitude-coupling on a slow temporal scale without necessarily causing phase-coupling. On the other hand, synaptic interactions triggered by intrinsic activity or sensory inputs may induce phase-coupling between areas without driving identical amplitude co-modulations (Landau et al., 2015). The notion of different mechanisms underlying both coupling modes is also supported by their distinct temporal dynamics (Daffertshofer et al., 2018).

Notably, also residual non-neuronal signals, such as e.g. muscle activity, eye-movements or cardiac activity, might systematically affect both coupling modes. Such sources may induce or hamper reliable coupling patterns across subjects and coupling modes, and thereby, affect the correlation of coupling patterns between coupling modes.

3.4.4 Functional role of coupling modes

Phase-coupling of neuronal populations may regulate their interactions by aligning rhythmic excitability fluctuations and rhythmic inputs (Fries, 2015). Similarly, amplitude-coupling may modulate interactions by temporally aligning processing associated with low or high oscillatory amplitudes across brain regions (von Nicolai et al., 2014; Siegel et al., 2012). While the observed differences between coupling modes may reflect such functional roles, the present results hold independent from such potential functions. In

fact, even if phase- or amplitude-coupling merely reflect neural interactions without a causal mechanistic role, our results show that these coupling modes provide partially dissociated and thus non-redundant information about neuronal interactions. This suggests that both coupling modes provide complementary information on large-scale neuronal interactions during cognitive processes and on their alteration in neuropsychiatric diseases.

3.4.5 Limitations

Our results are based on the assumption of Gaussian signals. Deviations from this assumption may have an effect on two levels. First, non-Gaussian signals will lead to sub-optimal orthogonalization (Brookes et al., 2012, 2014; Hipp et al., 2012). Second, the spurious amplitude-coupling of non-Gaussian signals will deviate from the simulated estimates based on Gaussian signals. Thus, optimal estimation of spurious amplitude-coupling requires a further systematic assessment of the effect of signal distributions.

3.4.6 Conclusion

With our first empirical study (Siems and Siegel, 2020) we showed that cortical phase- and amplitude-coupling patterns are non-redundant (Hypothesis 1.2), which may reflect at least partially distinct neuronal mechanisms. These results are independent of the critical bias that induces spurious amplitude-coupling due to phase-coupling and highlighted and clarified the compound nature of amplitude-coupling measures (Hypothesis 1.1). We could draw these conclusions due to a newly established analysis approach combining empirical measurements and simulations. Additionally, our findings are unaffected by the non-uniform signal-to-noise ratio distribution.

4 Connectivity as a biomarker of pathology

Modern network science offers the opportunity to not only understand the functioning of the healthy but also the pathologically altered brain. A fostered understanding of normal brain function made it possible to address functional connectivity changes in various neurological and psychiatric disorders (cf.: Fornito et al., 2015; Heuvel and Sporns, 2019; Stam, 2014). Recent studies have applied functional connectivity measures as a versatile biomarker in autism (Kitzbichler et al., 2015), schizophrenia (Cetin et al., 2016; Maran et al., 2016), epilepsy (Burns et al., 2014; van Dellen et al., 2014; Zerouali et al., 2016), dementia (Koelewijn et al., 2017; Maestú et al., 2015), Parkinson's disease (Oswal et al., 2016) and blindness (Hawellek et al., 2013) among others.

As specific as these disease phenotypes are, associated changes on the network level appear to follow a specific set of rules: Wherever tissue damage or alterations occur the effect appears to progressively spread through the entire connectome (Fornito et al., 2015; Stam, 2014). This spread is supposed to be a result of the hierarchical organization of the brain (Crossley et al., 2014; Rubinov and Sporns, 2010). At the top of the hierarchy are so-called rich-club nodes, a selection of nodes that form strong connections and facilitate effective long-range communication (Rubinov and Sporns, 2010). Lower down the hierarchy are the modules that are related to the direct processing of information.

Theoretically, a primary pathological area will affect its connected nodes and increase or decrease their function. If the secondarily affected nodes cannot compensate for the altered input, those changes will spread higher up the hierarchy (Fornito et al., 2015; Heuvel and Sporns, 2019; Stam, 2014). Changes to nodes on the highest level of the hierarchy, i.e. the "rich-club", likely lead to the strongest pathological and behavioral effects (Crossley et al., 2014).

4.1 Functional connectivity in Multiple Sclerosis

Multiple Sclerosis (MS) is an inflammatory, demyelinating secondary neurodegenerative disease (Dendrou et al., 2015). From early disease stages on and during disease progression (Amato et al., 2010), accumulating white-matter lesions and cortical atrophy can lead to cognitive decline and physical disability (Chiaravalloti and

DeLuca, 2008). While gross white-matter damage itself is only weakly related to disease severity and duration (Benedict and Zivadinov, 2011; Benedict et al., 2004; Stam, 2014), fine-grained analyses of structural connectivity and neuronal coupling revealed that the location of affected white-matter tracts is pivotal (Schoonheim et al., 2015; Stam, 2014). Using Magnetic Resonance Imaging (MRI), Magnetoencephalography (MEG) and Electroencephalography (EEG), anatomical and functional network changes have been related to tissue pathology (Roosendaal et al., 2009; Shu et al., 2011; Tewarie et al., 2014a), cognitive deficits (Cogliati Dezza et al., 2015; Gschwind et al., 2016; Hardmeier et al., 2012; Hawellek et al., 2011; Rocca et al., 2012; Schoonheim et al., 2013; Sjøgård et al., 2021; Tewarie et al., 2013, 2014b), clinical subtypes (Kocevar et al., 2016) and disease duration (Liu et al., 2016).

The high temporal resolution of MEG and EEG allows to characterize the frequency specific coupling of neuronal activity, which may reflect (Hipp and Siegel, 2015; Siegel et al., 2012) and even mediate (Fries, 2005) interactions in large-scale brain networks. Accordingly, electrophysiological studies in MS patients have revealed changes of neuronal coupling in specific frequency ranges (Hardmeier et al., 2012; Schoonheim et al., 2013; Tewarie et al., 2013, 2014a). While these studies have largely focused on phase-coupling as a measure of functional connectivity, recent findings have highlighted amplitude-coupling as another mode of neuronal interactions that may provide robust connectivity information, non-redundant to phase-coupling (Brookes et al., 2012; Daffertshofer et al., 2018; Hipp et al., 2012; Siems and Siegel, 2020; Siems et al., 2016; Sjøgård et al., 2021; Wens et al., 2014). However, so far it is unknown how such amplitude-coupling changes may relate to phase-coupling.

Additionally, the change in cognitive function can be related to both increased and decreased connectivity (Hardmeier et al., 2012; Hawellek et al., 2011; Tewarie et al., 2013). Human electrophysiology studies in particular paint a complex picture of connectivity progression. Here, the sign of connectivity changes strongly depends on the isolated carrier frequency of the signal (Hardmeier et al., 2012; Schoonheim et al., 2013; Tewarie et al., 2013, 2014a). Moreover, disease duration appears to be an important factor for network changes and might depend on the interplay of gray and white-matter damage (Tewarie et al., 2018b). Hence, it appears critical to identify compensatory mechanisms of brain connectivity over the course of the disease to understand their function and more generally learn about brain connectivity organization itself.

5 Altered cortical phase- and amplitude-coupling in Multiple Sclerosis

5.1 Scientific questions and aims

In our second study (Siems et al., 2021) we assessed if we can classify Multiple Sclerosis patients from healthy controls based on their electrophysiological coupling networks. In contrast to the recent literature our sample comprised a relatively early disease stage (median EDSS = 1.5, range 0 to 3.5). So far most studies applied only phase-coupling measures to assess disease specific alterations of functional networks (Cover et al., 2006a; Hardmeier et al., 2012; Schoonheim et al., 2013; Tewarie et al., 2013, 2014b; Van Schependom et al., 2014a) and little is know about the changes in amplitude-coupling (Sjøgård et al., 2021). We thus focused our analyses on both amplitude- and phase-coupling networks and their interactions. As we have outlined in our first study these two coupling modes dissociate in the healthy brain and might indicate at least partly distinct neuronal mechanisms (Avramiea et al., 2021; Daffertshofer et al., 2018; Siems and Siegel, 2020). The question remained if the two coupling modes do further dissociate in the diseased brain.

Here, we measured magnetoencephalography (MEG) of 17 relapsing-remitting Multiple Sclerosis patients (Lublin and Reingold, 1996; Polman et al., 2011) and 17 healthy controls. The patient group was measured prior to the first application of Tecfidera (dimethyl fumarate; BioGen Inc., Cambridge, MA, USA) with median disease durations of 1 month (0 - 3 years interquartile range, maximum 11 years). Multiple Sclerosis is a progressive neurological disease that through demyelination primarily affects the structural basis of connectivity. However, the demyelinating effects of Multiple Sclerosis can occur diffusely and the lesions will likely not overlap between subjects. Nonetheless, recent disease models proposed that areas and connections higher up the connectomic hierarchy, so-called hubs, might show generalized effects (Fornito et al., 2015; Heuvel and Sporns, 2019; Stam, 2014). Hereby, it has been shown that neurological tissue damage does not solely lead to a lack or decrease of coupling but can as well show an increase in coupling as a result of compensatory effects (Hawellek et al., 2011; Schoonheim et al., 2013, 2015; Tewarie et al., 2018b). Addressing the inter-

subject variability was one of the major challenges of this study, particularly due to the high-dimensional search space of functional connectivity.

Here, we tried to answer two main questions addressing all of the above-mentioned points. First, we tried to establish a lower-dimensional feature-space in which the successful classification between patient and control group was possible. Second, we assessed if the feature characteristics differ between amplitude- and phase-coupling networks and show a dissociated spatio-spectral structure.

5.2 Materials and methods

5.2.1 Subjects and dataset

We analyzed MEG data from two datasets. The first dataset was recorded at the MEG-Center Tübingen and included eyes-open resting-state MEG measurements from 34 subjects. 17 of these subjects (8 female, mean age (± std) 31.1 ± 9.6 years) were diagnosed with RRMS and 17 subjects were healthy controls (9 female, mean age (± std) 28.4 ± 4.2 years, p = 0.30). The patient group was measured prior to the first application of Tecfidera (dimethyl fumarate; BioGen Inc., Cambridge, MA, USA) with a median disease duration of 1 month (0 - 3 years interquartile range, maximum 11 years). Neurological impairment was assessed with the Expanded Disability Status Scale (Kurtzke, 1983; n = 14; median $EDSS_{total}$ = 1.5, range 0 to 3.5) and the Multiple Sclerosis Functional Composite (Fischer et al., 1999; n = 13; median $MSFC_{totalz}$ = -1.8, range -0.3 to -3.3). All participants gave written informed consent in accord with the Declaration of Helsinki, and the study was approved by the ethics committee of the medical faculty of the University of Tübingen.

We collected 10 minutes of eyes-open resting-state MEG data per subject. The MEG was continuously recorded with a 275-channel whole-head system (Omega 2000, CTF Systems Inc., Port Coquitlam, Canada) in a magnetically shielded room. The head position was tracked using three head localization coils fixated at the nasion and the left and right preauricular points. MEG signals were recorded with 2343.75 Hz sampling frequency and down sampled to 1000 Hz offline.

A T1-weighted sagittal MRI was obtained from each participant to construct individual high-resolution head models (MPRAGE sequence, TE = 2.18 ms, TR = 2300 ms, TI = 1100 ms, flip angle = 9°, 192 slices, voxel size = 1 × 1 × 1 mm). The subjects were

scanned in a Siemens MAGNETOM Trio 3T scanner (Erlangen, Germany) with a 32-channel head coil.

The second dataset included 95 subjects from the publicly available human connectome project (HCP) S900 release (Larson-Prior *et al.*, 2013). Participants were healthy adults in the age range between 22-35 years ($n_{22\text{-}25}$ = 18, $n_{26\text{-}30}$ = 40, $n_{31\text{-}35}$ = 37). The HCP-sample included 45 females. The HCP-MEG data included three six-minute blocks of eyes-open resting-state MEG with short breaks in between measurements. Data were recorded with a whole-head Magnes 3600 scanner (4D Neuroimaging, San Diego, CA, USA) situated in a magnetically shielded room (for further details see: Larson-Prior et al., 2013). Additionally, the HCP-subjects were scanned on a Siemens 3T Skyra to acquire structural T1-weighted magnetic resonance images (MRI) with 0.7mm isotropic resolution (Van Essen et al., 2013).

5.2.2 Data preprocessing

For the Tübingen-dataset, we first notch-filtered line noise at 50 Hz and at the first six harmonics (stop-band width: 1 Hz). Second, we visually inspected the data for muscle-, eyeblink-, and technical artifacts (SQUID-jumps). We rejected corresponding time intervals and malfunctioning or noisy channels (mean: 1 channel; range: 0 to 3 channels). Third, we high-pass filtered the data at 0.5 Hz with a 4^{th}-order zero-phase Butterworth filter and split the data into two frequency bands: a low frequency band from 0.5–30 Hz and a high frequency band with frequencies above 30 Hz. For both frequency ranges, we separately performed independent component analysis (ICA) (Hyvärinen and Oja, 2000). This approach takes advantage of the distinct spectral profile of different physiological artifacts, such as muscle and eye-movement artifacts (Hipp and Siegel, 2013). For both frequency ranges, independent components were visually inspected and artifactual components were rejected according to their topology, time course and spectrum (Chaumon et al., 2015; Hipp and Siegel, 2013). Finally, both frequency bands were recombined.

For the HCP-dataset we used the preprocessed data as provided by the HCP pipeline (Larson-Prior et al., 2013). This included removal of noisy and malfunctioning channels, bad data segments and physiological artifacts by the iterative application of temporal and spatial independent component analysis (ICA; Larson-Prior et al., 2013; Mantini et al., 2011).

5.2.3 Physical forward model and source modeling

MEG sensors were aligned to the individual anatomy using FieldTrip (Oostenveld et al., 2010). We segmented the individual T1-weighted images and generated a single shell head model to compute the physical forward model (Nolte, 2003) for 457 equally spaced (~1.2 cm distance) source points spanning the cortex at 0.7 cm depth below the pial surface (Hipp and Siegel, 2015; Hipp et al., 2011b; Siems and Siegel, 2020). The source shell was generated in MNI-space and non-linearly transformed to individual headspace. We co-registered the source coordinates, head model and MEG channels on the basis of the three head localization coils.

The sensor-level MEG data was projected to source space using linear beamforming (Gross et al., 2001; Van Veen et al., 1997). This spatial filtering approach reconstructs activity of the sources of interest with unit gain while maximally suppressing contributions from other sources.

5.2.4 Spectral analysis

We generated time-frequency estimates of the time-domain MEG signal using Morlet wavelets (Goupillaud et al., 1984). The bandwidth of the wavelets (1 spectral standard deviation) was set to 0.5 octaves with a temporal step-size of half the temporal standard deviation. We derived spectral estimates for 23 frequencies from 2.8 to 128 Hz in quarter-octave steps.

5.2.5 Neuronal Coupling

We estimated neuronal amplitude- and phase-coupling by means of amplitude envelope correlations of orthogonalized signals (Hipp et al., 2012) and the weighted phase lag index (Vinck et al., 2011), respectively. Importantly, both measures are insensitive to volume conduction and might relate to distinct functional mechanisms of cortical network interactions (Daffertshofer et al., 2018; Engel et al., 2013; Siegel et al., 2012; Siems and Siegel, 2020). For the application of amplitude-coupling we used pairwise orthogonalization of the two complex signals at each time-point (Brookes et al., 2012; Hipp et al., 2012) before correlating the log-transformed power envelopes.

For both metrics all subjects and frequency bands, we generated full and symmetric correlation matrices. For further analyses, we vectorized all unique connections of these correlation matrices. We refer to the resulting vectors as coupling profiles.

5.2.6 Direct comparison of coupling

For every connection (n_c = 104,196) in each frequency band (n_f = 23), we tested for group differences in coupling strength (two-tailed Mann-Whitney U-tests) and applied false-discovery rate correction (Benjamini and Hochberg, 1995) for multiple-comparison correction within each frequency. Further, we tested which group was more likely to show stronger coupling in each frequency band by testing the distribution of the sign of significant t-scores ($p < 0.05$, corrected) against 0.5 using a binomial test. In other words, we tested the Null-hypothesis for the same probability of positive and negative signs. For the binominal statistic, we conservatively estimated the degrees of freedom at df = 40 as the rank of the forward model, i.e. the maximum amount of independently separable sources (compare Hipp and Siegel, 2015; Wens et al., 2015). Furthermore, we FDR-corrected the results of the binomial tests across frequencies.

5.2.7 Dimensionality reduction of coupling spaces

In a first step, in the HCP dataset, for each frequency and coupling measure, we applied PCA to the coupling profiles across HCP subjects (n_{hcp} = 95) in order to identify components, i.e networks of coupling that explain most variability across subjects. Next, we projected the coupling profiles of the Tübingen patient and control subject dataset into the PCA space. For each frequency and both coupling modes, we multiplied the z-scored coupling profiles of every subject with the component eigenvectors of the PCA. In each frequency band, we used the 30 principle components with the highest eigenvalues, which resulted in 690 feature dimensions per coupling measure (coupling components).

5.2.8 Feature bagging and group classification

In a second step, we applied bootstrap aggregating (feature bagging) to identify the components that best separate between the two groups (Fig. 10A). We drew a random subset of features (n_{sub} = 10) from all 1380 features, classified the two groups using a support vector machine classifier with leave-one-out cross-validation, and repeated this procedure ($n_{draw} = 2x10^7$). As control analyses, we repeated the procedure for n_{sub} = 2, 3, 5, 20 and for three other classification algorithms (decision trees, linear discriminatory analysis, naïve Bayes classifier). This procedure resulted in a distribution of classification accuracies across random feature selections. We defined the features that

best separate between patients and controls by applying a threshold at the 75-percentile of this distribution (Fig. 10B). If no feature can classify between the two groups the probability of any feature to be in the subsets with the 25% highest accuracies will be equal. However, if features contain information to classify the two groups, this probability will increase. Thus, we defined the probability of a feature to be in the 25% subsets with the highest accuracies as its classification score. As control analyses, we repeated the analyses for different accuracy thresholds: 66%, 90% and 98% cutoff.

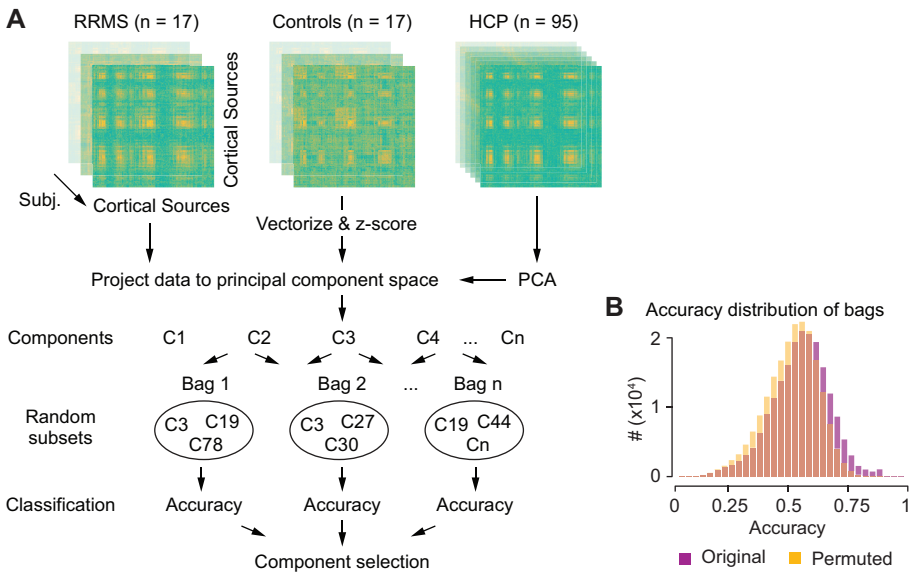

Figure 10. Analysis approach

(**A**) For each subject, coupling measure and frequency we computed complete cortico-cortical correlation matrices and vectorized and z-scored the upper triangle. We conducted PCA on the coupling vectors of the HCP data and projected the coupling vectors of RRMS-patients and control subjects into the resulting space of principal coupling components. We applied bootstrap aggregating (feature bagging) to identify coupling components that best classify between RRMS patients and control subjects. We drew random subsets of 10 components (bags) and, for each bag, classified (SVM) between groups with leave-one-out cross-validation. We employed a permutation statistic to select components that were more often in the top quartile of best classifying bags than expected by chance (see methods) (**B**) Distribution of classification accuracies across all $2x10^7$ bags for the original data (purple) and for randomly permuted group assignments of subjects (yellow).

5.2.9 Statistical testing of classification scores

We used permutation statistics to test the statistical significance of every feature's classification score, i.e., the likelihood of a given classification score under the Null-hypothesis that groups cannot be classified based on this feature. A significant feature indicates a spatio-spectral pattern of cortical coupling that separates between patient and control groups.

For each permutation (n = 1000), we randomly reassigned subjects to one of the two groups, keeping the same ratio between groups and repeated our analysis. Importantly, for each permutation, we again drew $n_{draw} = 2x10^7$ feature bags per group permutation to account for the random separability of any group constellation. We then combined all classification scores (1000 permutations of 1380 feature-specific classification scores) to define one general, component-independent Null-distribution and to assign p-values for each classification score. We corrected these p-values with false-discovery rate correction across the 1380 scores (FDR-correction; Benjamini and Hochberg, 1995).

To test if groups could be significantly classified in general, we quantified how likely it was to find the identified number of significant components under the Null-hypothesis that groups could not be classified. We applied the same procedure as for the real data to every group permutation and quantified how many significant components we could identify ($p < 0.05$, FDR-corrected). The resulting distribution across the 1000 permutations served as the Null-distribution of significant components. All permutations had less significant features than identified for the real data (58 features). In fact, not more than one significant feature ($p < 0.05$, FDR-corrected) was identified for any of the 1000 permutations.

5.2.10 Classification confidence

We quantified classification confidence as a distant measure. For each subject *i*, we compared the Mahalanobis distance D_{mah} of its feature vector to the distribution of feature vectors for the patient and for the control group. We computed D_{mah} of subject i:

$$D_{Mah,i,g} = (f_i - \mu_g) * C_g^{-1} * (f_i - \mu_g)'$$

Here, *fi* describes the feature vector of each subject; μ and *C* describe the group *g* mean and group member covariance, respectively. We excluded the *ith* subject from the corresponding mean and covariance matrix calculation. The exponential *-1* indicates

matrix inverse and the ‘ operator indicates the transpose. We then defined classification confidence as the difference between $D_{Mah,i,con}$ – $D_{mah,i,rms}$. Thus, a positive value indicates that a subject is closer to the patient group mean than to the control group mean and vice versa.

5.2.11 Spatial distribution of PCA components

The component coefficients derived from the HCP-dataset contain the spatial distribution of each principal component. However, the sign of these weights is inherently ambiguous. We achieved sign consistency across components by sign flipping those components for which the mean component scores within the patient group were smaller than in the control group. Hence, a positive component coefficient indicates that the coupling is relatively increased in patients whereas a negative coefficient indicates a coupling decrease.

We visualized the spatial distribution of PCA components as the average of all normalized significant components within a frequency band and coupling measure: delta (2.8 - 3.4 Hz), theta (4 - 6.7 Hz), alpha (8 - 13 Hz), beta (16 - 27 Hz), low gamma (32 - 54 Hz) and high gamma (64 - 128 Hz). For the normalization we divided each component by the absolute 98th-percentile across all its connections.

5.2.12 Unbiased accuracy estimation

To estimate the unbiased accuracy with which any new subject can be classified as patient or healthy control, we employed a second-level leave-one-out cross-validation. Leaving out each subject at a time, we applied the complete analysis pipeline outlined above, defined features spaces, and classified the left out subject.

We generated a continuous estimate of accuracy by computing the distance of the left-out subject from the decision boundary. To compare distances across different feature space realizations, i.e. left out subjects, we defined distances in units of standard deviation. We divided the distance of the left-out subject in each feature space by the standard deviation of the distances to the decision boundary of all but the left-out subjects. The sign of the distance was set positive or negative if the subject was classified as a patient or healthy control, respectively.

Finally, we separately fit a Gaussian distribution to the patient (N_{MS}) and healthy control group (N_{con}) distances. We derived the unbiased sensitivity, specificity and accuracy of classification from these two Gaussians:

$$sensitivity = \int_{0}^{+\infty} N_{rrms} \Big/ \int_{-\infty}^{+\infty} N_{rrms}$$

$$specificity = \int_{-\infty}^{0} N_{con} \Big/ \int_{-\infty}^{+\infty} N_{con}$$

$$accuracy = \frac{1}{n_{all}}(n_{rrms} * sensitivity + n_{con} * specificity)$$

where $\int$ indicates the integral and the two Gaussians, N_{MS} and N_{con}, are defined by the group specific mean and standard deviation. The group sizes were defined by n_{MS}, n_{con} and n_{all} for the patient group, the control group and all subjects, respectively.

5.3 Results

We compared brain-wide phase- and amplitude-coupling of frequency specific neuronal activity between 17 patients diagnosed with RRMS and 17 healthy control subjects. Cortical phase- and amplitude coupling was estimated from 10 min of eyes-open resting-state MEG measurements. We reconstructed cortical activity from the MEG using beamforming (Gross et al., 2001; Van Veen et al., 1997) and quantified phase- and amplitude-coupling using the weighted phase-lag index (Vinck et al., 2011) and power-correlations of orthogonalized signals(Hipp et al., 2012), respectively. Both measures are insensitive to volume conduction (Brookes et al., 2012; Hipp et al., 2012; Vinck et al., 2011) and show strong intra- and inter-subject reliability (Colclough et al., 2016; Hipp et al., 2012; Siems and Siegel, 2020; Siems et al., 2016; Wens et al., 2014).

5.3.1 Direct comparison of neuronal coupling

As a first approach, we directly compared the connection- and frequency-wise coupling between patients and controls (Fig. 11; n_c = 104,196; n_f = 23). While differences between groups peaked around 19 Hz and 45 Hz for amplitude- and phase-coupling, respectively (Fig. 11, purple lines), these effects were not statistically significant when applying false discovery rate-correction for the number of connections tested (Fig. 11,

green lines). This highlights how the high dimensionality of brain-wide coupling impedes a direct statistical comparison.

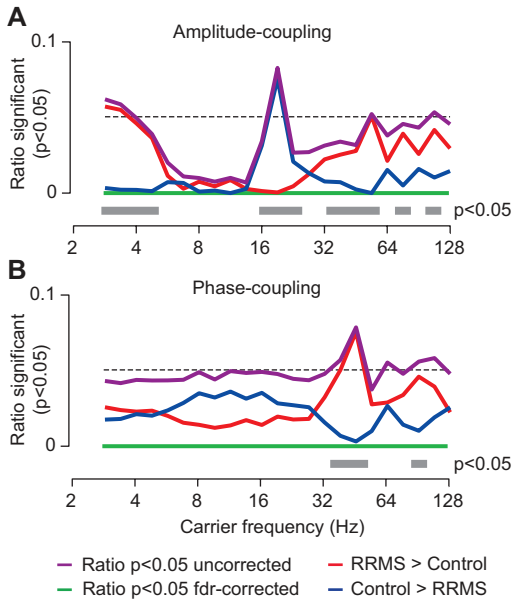

Figure 11. Connection-wise comparison of neuronal coupling between MS patients and control subjects

(**A**) Amplitude-coupling (orthogonalized amplitude correlations) (**B**) Phase-coupling (weighted phase-lag index). In both panels, the purple line indicates the ratio of significantly different connections ($p < 0.05$ uncorrected) and the green line indicates this ratio after false-discovery rate correction. The red and the blue lines show the ratio of connections with increased and decreased coupling in the patient group, respectively ($p < 0.05$, uncorrected). The gray bars display carrier frequencies with a significantly directed ratio of effects ($p < 0.05$, FDR-corrected), i.e. more connections with significantly increased or decreased coupling. The black dashed line indicates 0.05.

Nevertheless, the direct comparison revealed an intriguing pattern of the sign of differences between groups (Fig. 11, red and blue lines). If there was no difference between groups, the sign of randomly significant differences in coupling (type I errors) would be equally probable in both directions. However, the observed differences deviated from this distribution for both coupling measures (Fig. 11, gray bars). For amplitude-coupling, patients showed decreased coupling in the beta frequency range (16 – 22 Hz) and increased coupling in the delta (2 – 4 Hz) and gamma (32 – 106 Hz)

frequency ranges. Phase-coupling in patients was increased in the low gamma frequency range (38 – 54 Hz).

In summary, although the vast number of connections impaired the direct comparison of coupling on the connection-level, the asymmetry of observed differences suggested that there are systematic and frequency-specific differences of coupling between early-stage MS patients and healthy control subjects.

5.3.2 Group classification based on principal coupling components

To overcome the limitations of the connection-wise analysis and to efficiently cope with the high dimensionality of the brain-wide coupling space, we next devised a multistage machine-learning approach (Figure 10). In brief, we first identified a subspace of principle coupling components in an independent MEG dataset, then projected the patient and control data into this coupling space, and finally employed a bootstrapped classification approach to identify significant coupling differences between groups.

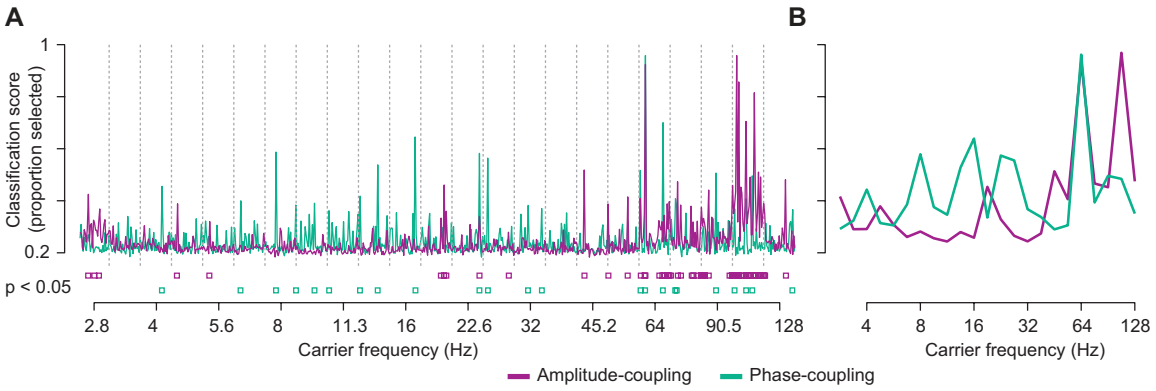

Figure 12. Selection of principal coupling components by classification scores
Classification scores were defined as the likelihood of each component to contribute to bags with classification accuracies in the top quartile of all $2x10^7$ bags. (**A**) Classification scores for all 30 amplitude- (purple) and phase-coupling (green) components of each carrier frequency ordered by the variance explained within each frequency. The components and eigenvalues were derived from the HCP-dataset. Dashed lines divide the carrier frequencies. Purple and green squares indicate significant classification scores for amplitude- and phase-coupling components, respectively ($p < 0.05$, FDR-corrected) (**B**) Maximum classification scores per carrier frequency for amplitude- (purple) and phase-coupling (green).

To efficiently reduce the dimensionality of the coupling space, we applied principal component analysis (PCA) to the z-scored brain-wide phase- and amplitude-coupling of 95 subjects from the human connectome project S900 MEG dataset (Larson-Prior et al., 2013). For each frequency and both coupling modes, we extracted the 30 principal coupling components that explained most variability of coupling across subjects (largest eigenvalues). Importantly, the identification of principal coupling components in an independent dataset ensured, that this identification itself was not conflated by any potential variability between patient and control groups. We next projected the coupling profiles of patients and control subjects into the principal coupling space, which resulted in a more than 3000-fold dimensionality reduction to a total of 1380 coupling components.

We next employed multivariate classification (support vector machine, SVM) to identify significant differences of coupling between groups in the reduced coupling space. Because likely not all components are informative, classification accuracy suffers when utilizing all components at once (Pappu and Pardalos, 2014). Similarly, by using every component for itself, generic interactions between components and frequencies might be missed. We therefore employed a bootstrap approach (feature bagging). 20-million times, we picked a random subset of 10 coupling components (without replacement) and applied SVM to classify patients and controls with leave-one-out cross-validation (Fig. 10A). For each component, we then computed a classification score as its likelihood to contribute to component-subsets with classification accuracies in the top quartile (Fig. 10B). For each component, we statistically tested its classification score using a permutation approach ($p < 0.05$, FDR-corrected). This procedure allowed us to identify 58 coupling components that significantly contributed to the classification of patient and control groups (Fig. 12A, $p < 0.05$ FDR-corrected). 34 and 24 of these components were specific to amplitude-coupling and phase-coupling, respectively.

The employed permutation statistic also allowed us to test whether overall we could significantly classify between the two groups. We quantified how likely it was to find the identified number of significant components under the Null-hypothesis that groups could not be classified. We found that the amount of identified features was indeed highly significant ($p < 0.001$). Thus, early-stage MS patients could be significantly classified

from healthy control subjects based on a specific set of principal phase- and amplitude-coupling components.

These results were robust across a broad range of parameter choices and control analyses. First, we repeated the analysis separately for amplitude- and phase-coupling components. The classification scores were similar and well correlated to those obtained when combining amplitude- and phase-coupling components (amplitude-coupling $r = 0.79$; phase-coupling: $r = 0.65$). We further repeated the analyses for different bag sizes (2, 3, 5, 20), accuracy thresholds (0.66, 0.9, 0.98), and classification algorithms (naïve Bayes, decision tree and linear discriminatory analysis). The results were again very similar with high correlations of classification scores between approaches (bag size: $0.92 < r < 0.96$; accuracy threshold: $0.81 < r < 0.99$; algorithm: $0.65 < r < 0.91$; all $p < 0.05$, FDR-corrected across all comparisons).

5.3.3 Spectral and cortical distribution of altered coupling

We further examined the spectral and cortical distribution of coupling components that dissociated MS patients from healthy controls. For amplitude-coupling, these components were spectrally specific to low frequencies (< 5 Hz), the beta frequency range (19 Hz) and the gamma frequency range (> 40 Hz; Fig. 3B). For phase-coupling the classification score distribution showed several peaks in the theta (4 Hz), alpha (8 Hz), beta (13 - 16 Hz & 22 - 26 Hz) and gamma frequency range (> 45 Hz) (Fig. 12B).

To visualize the brain regions whose coupling dissociated patients from control, we first averaged the absolute coupling coefficients of all significant components for each brain region for frequencies below and above 35 Hz and both coupling measures (Fig. 13A). We split these frequency ranges because at frequencies above 35 Hz coupling estimated from MEG strongly resembles residual muscle activity (Hipp and Siegel, 2013; Siems et al., 2016).

We found that, for frequencies below 35 Hz, early-stage MS affected intra- and interhemispheric amplitude-coupling of the medial prefrontal, dorsolateral prefrontal, pericentral, lateral parietal and extrastriate visual cortex (Fig. 13A). For phase-coupling differences in this frequency range between patients and controls peaked in bilateral pericentral, inferior temporal and medial occipito-parietal areas, mainly with altered intra-hemispheric coupling. For high frequencies above 35 Hz, for both coupling modes, we

found differences between patients and controls for areas typically related to residual muscle-activity, that is bilateral anterior temporal and ventral frontal regions (Fig. 13A).

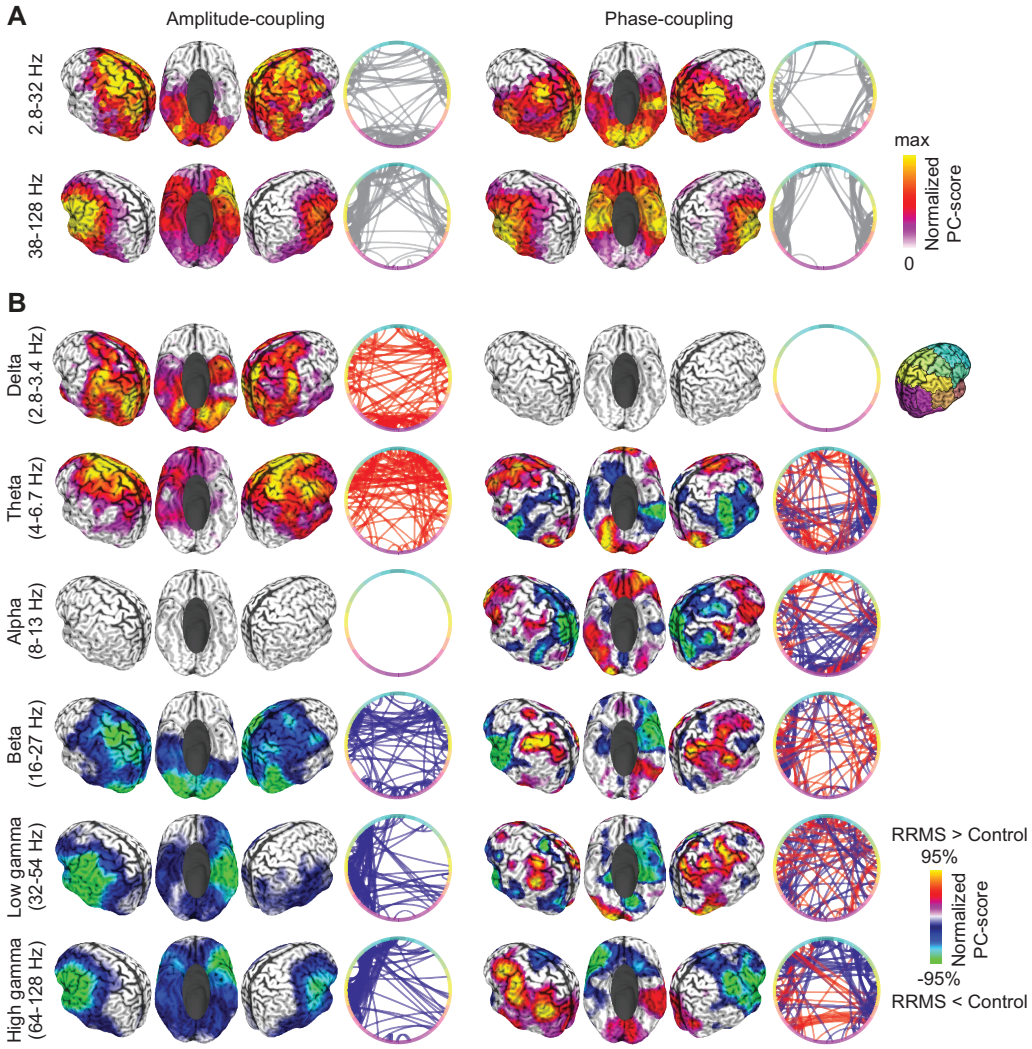

Figure 13. Cortical distribution of classifying coupling components

(**A**) Normalized average absolute strength of significantly classifying components for amplitude- (left) and phase-coupling (right), and for frequencies below (top) and above (bottom) 32 Hz. Colors are scaled between 0 and maximum for each panel. The circular line plots indicate connections with best classification between patients and controls (random subset of best 10%). The colors along the circle indicate cortical location, as shown on the right. (**B**) Normalized average strength of significantly classifying components for individual frequency bands and both coupling modes. Colors are scaled between the positive and negative absolute 95-percentile for each panel. Warm and cold colors indicate an increased and decreased coupling in patients, respectively. Circular line plots as in (A).

We next resolved the signed changes of coupling in patients within each frequency band (Fig. 13B). For amplitude-coupling, patients showed enhanced low-frequency coupling in lateral parietal and extrastriate visual areas in the delta band (2.8-3.4 Hz) and in medial and ventrolateral prefrontal cortex in the theta band (4 - 6.7 Hz). In the beta band (16-27 Hz), patients showed reduced amplitude-coupling in pericentral and visual areas. Frequencies above 32 Hz showed reduced amplitude-coupling in often muscle confounded anterior temporal and ventral prefrontal regions. Phase-coupling showed a rich pattern of changes in MS patients with typically bilateral increases and decreases of coupling within the same frequency range. Patients showed increased phase-coupling in medial prefrontal (theta, 4 - 6.7 Hz), lateral prefrontal (theta, alpha, beta & low gamma 8 - 54 Hz), as well as pericentral and lateral parietal areas (beta & gamma, 16 - 128 Hz). Phase-coupling was decreased in temporal (theta 4 - 6.7 Hz), medial and lateral parietal (alpha 8 - 13 Hz) as well anterior temporal areas (beta & gamma 16 - 128 Hz).

In summary, MS patients showed both, increased and decreased phase- and amplitude-coupling across a broad but highly specific range of frequencies and cortical regions.

5.3.4 Altered coupling predicts disease severity

If the identified changes of neuronal coupling in MS patients reflected disease-specific mechanisms, they may predict disease severity and our results support this hypothesis. We tested if, across patients, the confidence of classification based on neuronal coupling, i.e. how similar coupling was to that of patients as compared to controls, was correlated with two clinical measures of disease strength: the Expanded Disability Status Scale (Kurtzke, 1983) and the Multiple Sclerosis Functional Composite (Fischer et al., 1999). We found that indeed both clinical scores were significantly correlated with classification confidence (Fig. 14) (MSFC: $r = 0.49$, $p = 0.02$, FDR-corrected; EDSS: $r = 0.45$, $p = 0.04$, FDR-corrected). Thus, stronger coupling changes predicted a more severe disease state.

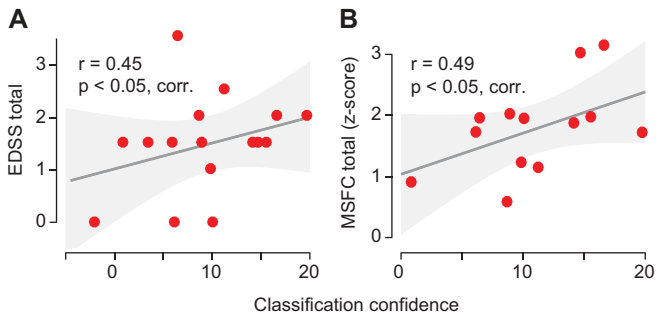

Figure 14. Correlations between classification confidence and behavioral scores of disease severity

Correlation between classification confidence and (A) the EDSS (Expanded Disability Status) and (B) the MSFC-scores (Multiple Sclerosis Functional Composite). The y-axis indicates the disease severity such that an increasing value corresponds to a more severe disease state. For MSFC we mirrored the values into the positive range to fit this notation (original values $MSFC_z$ = -0.3 - 3.3). Shaded areas are 95% confidence intervals of the linear model parameters.

5.3.5 Classification accuracy

In a final set of analyses, we quantitatively addressed the question how well novel early-stage MS patients could be classified based on the cortical coupling assessed with MEG. Importantly, the classification accuracy of an individual subjects based on the principal coupling components identified including this subject is positively biased. Thus, to derive an unbiased estimate of classification accuracy for a novel MEG dataset, we performed a cross-validation of the entire analysis pipeline leaving out and classifying each subject at a time. We performed this analysis for all combined coupling components (n_{comp} = 1380) as well as separately for the two coupling modes (n_{comp} = 690) and frequency ranges ($n_{comp,low}$ = 480 & $n_{comp,high}$ = 210).

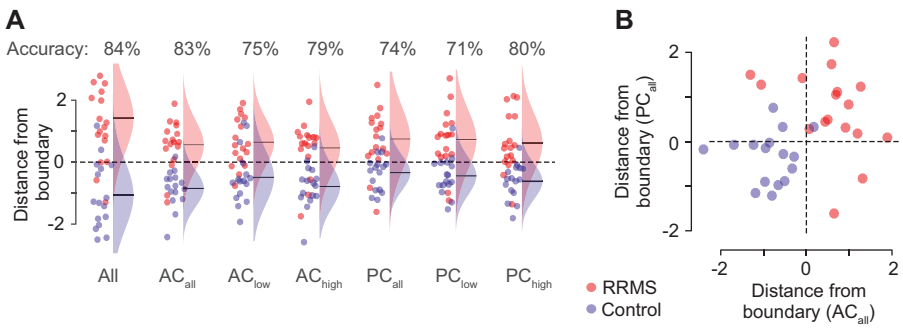

Figure 15. Classification accuracy

(**A**) Distance of every subject from the decision boundary (classification confidence) and Gaussian fits of the group distributions. Distances are normalized by the standard deviation across all subjects within each cross-validation fold. The circle color indicates the group; red for RRMS-patients and blue for controls. Frequencies are split below 35 Hz (low vs. high). (**B**) Each subjects' distance from the classification boundary for all amplitude- and phase-coupling components. AC (amplitude-coupling); PC (phase-coupling).

The unbiased classification accuracy using all coupling components was 84 % (chance level: 50%) and nominally higher than the accuracy obtained using any coupling mode or frequency range alone (Fig. 15A). The independent classification accuracy for amplitude-coupling (83 %) was higher than for phase-coupling (74%). Furthermore, we found that the distance to the classification boundary was only weakly correlated between amplitude- and phase-coupling ($r = 0.21$, $p > 0.05$) (Fig. 15B). In line with the enhanced accuracy when combining both coupling modes, this is supporting evidence for non-redundant information of phase- and amplitude-coupling.

5.4 Discussion

This study provides, to our knowledge, the first systematic comparison of brain-wide phase- and amplitude-coupling in Multiple Sclerosis patients. We identified several principal coupling components, which could significantly classify patients from healthy controls with an overall accuracy of 84% and with classification confidence predicting disease severity. For both coupling modes, in RRMS patients we found both, increased and decreased coupling across a broad range of frequencies and cortical regions. At higher frequencies, effects likely at least partially reflected changes in muscle activity (Hipp and Siegel, 2013; Siems et al., 2016). In summary, our results show systematic, wide-spread and non-redundant changes of phase- and amplitude-coupling in Multiple Sclerosis.

5.4.1 Classification approach

We employed a novel unsupervised multivariate classification approach that combines several key methodological advantages. First, all analyses were carried out on reconstructed cortical activity, rather than on the raw MEG-signals. This allowed to align subjects and enhanced the signal-to-noise ratio by rejecting non-neuronal activity and focusing on signals of neuronal origin (Hipp and Siegel, 2013; Van Veen et al., 1997). Furthermore, we employed phase- and amplitude-coupling measures that rejected spurious coupling due to field spread.

Second, we combined dimensionality reduction and bootstrap aggregating to classify between groups in a very high-dimensional dataspace. Critically, the dimensionality reduction was based on a large and completely independent dataset. Thus, the identified principal coupling components reflected universal characteristics of cortical coupling across human subjects independent from the variance between the two groups at hand. In turn, the identified components can be readily applied to any new dataset and question at hand. We employed a bootstrap approach (feature bagging) (Tin Kam Ho, 1998) to identify several relevant dimensions in the reduced dataspace. The results were similar across a broad range of bootstrap parameters (bag size, threshold) and classification algorithms, supporting the robustness and broad applicability of this approach.

Third, cross-validation at two critical stages ensured the generalization of results at the population level. First, we cross-validated (leave-one-out) the classification between

groups for every bootstrap aggregate of coupling components. This prevented overfitting for the identification of classifying coupling components. Second, we cross-validated (leave-one-out) the classification accuracy of the entire analysis pipeline, which ensured an externally valid and unbiased estimate of the classification accuracy for new datasets.

High dimensional feature spaces are a common problem in brain-connectivity analyses and biomedical research in general. Classification of groups of samples on the entire space is often not feasible because of uninformative dimensions and classification on individual dimensions may be computationally impractical, might miss multivariate interactions, and is difficult to control for multiple comparisons (Pappu and Pardalos, 2014; Hipp and Siegel, 2015; Wang *et al.*, 2018). In the present case, this is well illustrated by the failure to detect significant coupling changes in a direct connection-level comparison. In these situations, the new analyses approach employed here provides a flexible tool that can be readily adapted to classify comparably small samples in a high-dimensional space.

5.4.2 Wide-spread bidirectional changes of cortical coupling

Our results provide new insights into the spatial and spectral distribution of cortical coupling changes during early-stage MS. We found altered coupling across the entire investigated frequency range (2.8 to 128 Hz). This adds to a growing but heterogenous body of studies that have identified MS-related changes of rhythmic neural activity or coupling across various different frequency bands (Cover et al., 2006b; Figueroa-Vargas et al., 2020; Hardmeier et al., 2012; Schoonheim et al., 2013, 2015; Schoonhoven et al., 2019; Tewarie et al., 2013, 2014b; Van Schependom et al., 2014b). For phase-coupling, our approach revealed both increases and decreases within the same frequency range. This may have contributed to the heterogeneity of previous findings and highlights the advantage of separating cortical networks at the source-level.

Rhythmic coupling at different frequencies reflects interactions in specific neuronal micro and macro-circuits (Donner and Siegel, 2011b; Siegel et al., 2012). The spectrally widespread nature of our findings suggests that MS leads to alterations across many different circuit interactions. This may entail not only local and large-scale cortico-cortical interactions, but also cortico-subcortical interactions. For example, the altered phase-coupling in the alpha frequency range found here may reflect altered cortico-thalamic

interactions associated with MS-related thalamic atrophy (Schoonhoven et al., 2019; Tewarie et al., 2013).

The observed broad spatial distribution of altered coupling across the cortex accords well with its broad spectral distribution. Changes involved both, local and large-scale coupling. In general, the affected cortical networks resembled the known association with specific frequency ranges, such as for example altered theta- or beta- coupling in midfrontal and sensorimotor regions, respectively. This suggests that MS alters the strength of interactions in common brain networks associated with specific frequencies. It remains to be determined, to what extent also the frequency of these interactions is affected (Schoonhoven et al., 2019).

At frequencies above 35 Hz, MS patients showed decreased frontotemporal coupling, which well resembled the reported distribution of residual muscle activity in EEG and MEG (Hipp and Siegel, 2013; Siems et al., 2016). Thus, the decreased high-frequency coupling may be due to decreased muscle activity, which may in turn result from both, the disease itself as well as from motivational differences between patients and control subjects.

Motivational or cognitive differences may generally contribute to classification results between patient and control groups. In this context, the finding that classification confidence predicts disease severity within the patient groups is particularly important. This finding suggests, that the identified changes indeed reflect disease specific effects rather than general motivational differences between patient and control groups.

Several different mechanisms may contribute to such disease specific changes. On the one hand, lesions of white-matter tracts may directly cause a reduced coupling of the connected neuronal populations. On the other hand, such reduced anatomical connectivity and functional coupling may induce a number of indirect effects. For example, the decoupled populations may be part of a larger neuronal network. Local decoupling in this network may lead to a global decrease of coupling, compensatory enhancement of coupling or a mere shift of the network dynamics. Similarly, changes within one network may again lead to both, decreases as well as increases of coupling in other brain networks (Fornito et al., 2015; Helekar et al., 2010; Heuvel and Sporns, 2019; Schoonheim et al., 2015; Stam, 2014). Importantly, all these changes could span a broad range of temporal-scales, which may even lead to opposite immediate and long-term effects of the disease.

The interplay of all these mechanisms may explain the wide-spread, complex and often bi-directional pattern of coupling changes observed here. The present results set the stage for future studies to disentangle the different mechanisms underlying these changes. For this, longitudinal investigations will be particularly important (Schoonheim et al., 2015), and it will be key to link the observed coupling changes to detailed anatomical and cognitive pathologies.

5.4.3 Coupling mode specific changes

Amplitude correlation of orthogonalized signals has recently been introduced as a robust and spectrally specific marker of cortical coupling (Hipp et al., 2012; Siems and Siegel, 2020; Siems et al., 2016). Consistent with other recent evidence (Sjøgård et al., 2021), our results show that cortical amplitude-coupling is systematically altered in RRMS patients already at an early disease stage. Moreover, our findings uncover markedly distinct changes for phase- and amplitude-coupling. There were more coupling components that dissociated the groups and higher classification accuracy for amplitude-coupling than for phase-coupling (amplitude/phase-coupling: 34/24 components; 83/74% accuracy). This suggests that coupling changes are more robust for amplitude-coupling.

Furthermore, while phase-coupling showed effects in all but the delta-band, amplitude-coupling was altered in all but the alpha-band. Effects were also spatially dissociated. Below 35 Hz, amplitude-coupling showed strongest changes in medial and lateral prefrontal cortex as well as in pericentral and medial parietal areas, while phase-coupling showed strongest effects in pericentral, medial occipitoparietal and inferior temporal cortex. Additionally, while amplitude-coupling showed either consistent increases or decreases of coupling within each band, phase-coupling showed bidirectional effects within each band. For frequencies above 35 Hz, amplitude-coupling showed higher sensitivity to residual muscle activity. Finally, we found that the two coupling modes showed different sensitivities to different subgroups of subjects.

Overall, our results show that phase- and amplitude-coupling are sensitive to at least partially distinct changes of cortical coupling in MS. Accordingly, while both coupling modes could independently dissociate patients from healthy controls, the combination of coupling modes increased classification accuracy. Our findings suggest that amplitude-coupling provides a robust biomarker of changes in large-scale network dynamics during

early-stage MS that may be synergistically combined with phase-coupling measures. Furthermore, the observed differences between coupling modes adds to converging evidence that at least partially distinct neuronal mechanisms underlie both coupling modes (Daffertshofer et al., 2018; Engel et al., 2013; Siegel et al., 2012; Siems and Siegel, 2020).

5.4.4 Conclusion

In summary, we devised a new analysis approach that combines dimensionality reduction and bootstrapped multivariate classification to identify disease-related neuronal coupling changes. Our approach can be readily adapted to other scientific questions, and thus, holds great potential for the comparison of groups in high-dimensional search spaces.

Our results uncover systematic changes of large-scale cortical phase- and amplitude-coupling at an early disease stage of Multiple Sclerosis. Changes were coupling-mode specific and included decreases as well as increases across wide-spread frequency ranges and cortical networks. Our results highlight non-invasive electrophysiological measures of neuronal coupling as powerful new biomarkers of relapsing-remitting Multiple Sclerosis.

6 Summary and conclusion

The studies summarized in this thesis describe previously unknown relations between amplitude- and phase-based coupling in the human brain (Siems and Siegel, 2020; Siems et al., 2021). Our results suggest that these two coupling modes indicate similar but non-redundant network interactions. We presented several lines of evidence supporting this hypothesis:

First, in accordance with Hypothesis 1.2, we have shown in a large sample of healthy subjects that amplitude- and phase-coupling patterns are similar albeit not identical. On average, one third of the variance in amplitude-coupling patterns could not be explained by phase-coupling. Importantly, this quantity is free of methodological issues regarding volume-conduction, spurious amplitude coupling and the signal-to-noise ratio distribution and thus confirmed our Hypothesis 1.1. Additionally, the identified differences between coupling modes are spatially and spectrally specific. This is in line with a growing body of literature suggesting that effective brain communication is multiplexed over several time-scales within and between areas (reviewed for example in: Engel et al., 2013; Siegel et al., 2012).

Second, in accordance with Hypotheses 2.1 and 2.2, in the abnormal brain the two coupling modes show distinct disease-specific features. We analyzed Multiple Sclerosis patients and discovered spectrally and spatially specific components that separate those from healthy controls. These components yielded spatially and spectrally non-redundant information for the two coupling modes.

We conclude that there exists a complex relationship between amplitude- and phase-coupling patterns. Both coupling modes display similarities but are not completely redundant. Importantly, the differences are non-uniformly and broadly distributed over the spectrum and the cortex and appear to be relevant in the healthy as well as the diseased brain. Choosing one of the two coupling measures for the analysis of electrophysiological coupling might affect sensitivity for particular neuronal processes. Nevertheless, our analyses are a non-exhaustive description of their relationship and we can only speculate what exact mechanisms underlie distinct amplitude- and phase-coupling patterns.

In the following we will discuss the key findings of both presented studies. We will highlight possible neuronal and non-neuronal mechanisms that might explain these findings and propose new approaches that might foster the understanding of coupling mode-specific cortical interactions.

6.1 Coupling similarities

One key finding of both our studies was that amplitude- and phase-coupling patterns share a substantial amount of variance in the healthy and in the diseased brain. We could quantify this similarity to account for more than 60% of shared variance in healthy subjects (Siems and Siegel, 2020). The variance shared is larger than it is unique to any coupling mode. In the following, we discuss several neuronal and non-neuronal characteristics of brain activity that might affect amplitude- and phase-coupling simultaneously.

On the one hand, common input to neuronal populations or sources will co-modulate their activity and will ultimately suggest that sources are coupled both in phase and amplitude. This input can be of neuronal origin, i.e. synaptic input from a third neuronal assembly, or non-neuronal, i.e. through source leakage of distant and close-by sources or non-neuronal artifacts. Of note, this common-input problem might lead to an overestimation of similarity. Accounting for these factors is important to further evaluate the similarity of phase- and amplitude-coupling patterns. Therefore, recently described multivariate, leakage-corrected connectivity algorithms might be useful (Basti et al., 2018; Colclough et al., 2015) but further research in this direction is needed.

On the other hand, synaptic interactions between neuronal populations may phase-lock their activity while simultaneously increasing neuronal activity (Fries, 2015; Womelsdorf et al., 2007), leading to a simultaneous increase of both amplitude- and phase-coupling. As described in the communication-through-coherence framework (Fries, 2015) the oscillatory excitation-inhibition cycle of a neuronal assembly describes a probability function for when an input can be most effective (Destexhe et al., 1999; Lopes da Silva, 2013; Singer, 2013). Therefore, if the input excites the receiving assembly at the right time in the cycle, interacting assemblies are coupled by their phase. Similarly, as the activity of the input assembly varies over time and several oscillatory cycles, the strength of excitation varies as well and with it the activity in the

receiving neuronal assembly (c.f. Schneider et al., 2020). In other words, interacting assemblies would exhibit both phase- and amplitude-coupling.

6.2 Coupling differences

As we have pointed out before, amplitude- and phase-coupling patterns share more than 60% of variance. Conversely, this means that functional networks exhibit on average more than 30% unique variance per coupling mode. Thus, amplitude- and phase-coupling patterns are non-redundant measures of functional coupling. We concluded that these dissociations might be at least partially the result of distinct neuronal mechanisms. In the following, we want to highlight multiple non-exclusive and non-exhaustive processes, from the circuit level to macro-scale interactions, which might explain these differences.

First, amplitudes may be co-modulated without affecting the underlying phase relations. Here, we propose mechanisms that indirectly affect the ability of neuronal assemblies to fire. For example, a recent modeling study (Krishnan et al., 2018) proposed that slow fluctuations of extracellular potassium show infra-slow dynamics similar to the time scale of amplitude dynamics (Hipp et al., 2012). They further present theoretical evidence of how these fluctuations may be linked via long-range structural connections, entailing connectivity. Another line of evidence relates neuromodulatory activity with widespread signal power modulations (van den Brink et al., 2019). It appears plausible that a spatially exhaustive modulation of the cortical excitation-inhibition balance might induce large-scale amplitude-coupling without directly affecting phase-locking between neuronal populations (Pfeffer et al., 2018, 2020).

Second, phase synchronization can occur without affecting the signal amplitudes. Here, we propose mechanisms that are more directly related to neuronal information transfer. For example, along the lines of the communication-through-coherence hypothesis, intrinsic activity and neuronal communication may trigger synaptic interactions while maintaining its spiking frequency (Fries, 2015). Another mechanism that has recently been suggested is the so-called phase-resetting or attentional reset (Landau and Fries, 2012; Landau et al., 2015). In this process, sensory input instantaneously reorganizes phase relations into a coherent state, analogous to the effect of the radiofrequency pulse in magnetic resonance imaging. Such a reset does not

necessarily affect the signal power and might be another mechanism dissociating amplitude- and phase-coupling.

Lastly, one alternative explanation might be that both coupling modes reflect the same underlying communication processes but are unequally non-linearly related to these. In our first paper we could exclude monotonous non-linear interactions but non-monotonous non-linear input-output functions remain a possible dissociating mechanism (cf. for example Snyder et al., 2018). Clearly, however, all the proposed mechanistic explanations are to a certain degree speculative and further research is needed to gather empirical evidence for their validity.

6.3 Invasive recordings

The studies presented in this thesis give a first overview over similarities and differences between amplitude- and phase-coupling networks. We can show that the underlying mechanisms may not be completely redundant but we cannot further qualify the nature of these processes. In the last part of this thesis we want to give an outlook on how the presented analyses might be used and expanded further. We propose a total of three complementary approaches to shed more light on potential underlying mechanisms.

A first step might be the comparison of these features using invasive data (local field potentials (LFP), spiking activity). In M/EEG recordings we measure the linear summation of highly synchronous neuronal firing on the scalp level (Baillet et al., 2001) far away from the signal source. Thus, invasive recordings, which are performed directly within neuronal tissue, may improve the investigation of coupling modes and their underlying mechanisms. One advantage is that invasive recordings yield higher confidence regarding the signal origin than source reconstruction algorithms. The LFP measured at an electrode can be localized comparatively well. Additionally, with adequate referencing the problem of signal leakage does not apply to invasive recordings. Consequently, the established compound nature of leakage corrected amplitude-coupling is not a factor and comparisons between coupling modes become methodologically more feasible.

However, invasive recordings are limited in their spatial coverage. So far it is not viable to invasively measure activity of the entire cortex of larger animals to get a

complete and systematic picture of neuronal interactions in terms of amplitude- and phase-coupling. A comparison of coupling modes will therefore be strongly affected by the general research question and electrode placement.

6.4 Task-specific activity and coupling

A second possibility to improve the mechanistic understanding of neuronal processes underlying different coupling modes might be the experimental manipulation of large-scale neuronal coupling.

As the brain might be working in several distinct states during rest, the possible mechanisms affecting functional connectivity could be as manifold (Quinn et al., 2019; Vidaurre et al., 2017, 2018). In contrast, task-dependent activity modulations might influence functional connectivity and coupling mode relations in a more hypothesis-driven manner (Engel et al., 2013; Siegel et al., 2012). Thus, with a suitable experimental design one might be able to further elucidate the relationship between amplitude- and phase-coupling networks. However, to the best of our knowledge, we do not know of an experimental paradigm that theoretically differentiates amplitude- and phase-coupling within the same frequency range. We can therefore only speculate about a suitable task potentially applying the aforementioned attentional resetting paradigms (Landau and Fries, 2012; Landau et al., 2015).

Further, regarding the analyses of task-dependent activity one important caveat has to be considered. As we have outlined in our first paper, increasing the power and thereby the signal-to-noise ratio will ultimately change the measured coupling even in the absence of true neuronal coupling differences. Any task-dependent change in connectivity needs to be dissociated from task-specific changes in power to not conflate true connectivity changes with improved measurement accuracy.

6.5 Coupling in the normal and abnormal brain

A third line of research to foster understanding of the mechanisms underlying amplitude- and phase-coupling networks is to assess those connectivity features in different pathological or malfunctioning brain states. In a well-defined disease model and with a good control group, deviations in connectivity can be attributed to pathological

processes, lesions and changes of normal neuronal activity (Fornito et al., 2015; Heuvel and Sporns, 2019; Stam, 2014).

Unfortunately, disease mechanisms and effects are rarely well circumscribed and patient populations might show high in-group variability, e.g. due to comorbidities. Another possibility is the artificial induction of disease-like states via pharmacological manipulation of normal brain function. As such, the manipulation of neuromodulatory systems appears to be a fruitful possibility to evoke controllable activity changes while monitoring its effect on functional connectivity measures (van den Brink et al., 2019; Pfeffer et al., 2020). Catecholamines, particularly norepinephrine, have been shown to affect the excitation-inhibition balance in local microcircuits, increasing the response of cortical neurons to synaptic input (Froemke, 2015; Murphy and Miller, 2003; Pfeffer et al., 2018, 2020; Polack et al., 2013). Such a mechanism would be in line with an increase in amplitude-coupling between distant brain regions but not necessarily lead to increased phase-coupling beyond the effects of signal-to-noise ratio improvements. However, empirical evidence for this notion is sparse and functional connectivity during pharmacological manipulation has so far mainly been assessed with functional magnetic resonance imaging (for example: van den Brink et al., 2016, 2018; Shine et al., 2018).

6.7 Conclusion

Overall, our studies contribute to the better understanding of large-scale neuronal interactions. We have shown that distinct signal components, namely the phase and the amplitude, reveal dissociated interaction patterns. Even though we applied well established measures of functional coupling (Brookes et al., 2012; Hipp et al., 2012; Vinck et al., 2011), the relationships between amplitude- and phase-coupling networks has not been assessed systematically before. We identified similarities and differences between both coupling modes that were widely distributed across the entire spectrum and cortex and found markedly affected networks in the diseased brain.

Additionally, a crucial proportion of the work presented here outlined, discussed and put forward solutions for methodological issues in electrophysiological functional connectivity analysis. These issues include signal leakage, non-uniform distributions of measurement error and signal-to-noise ratio, the compound nature of orthogonalized amplitude-coupling measures, as well as classification and statistical testing in high-dimensional data. We therefore consider the presented work as a valuable and general

guide for interaction analyses of cortical amplitude- and phase-coupling of non-invasive and invasive electrophysiological measurements.

7 References

Amato, M.P., Portaccio, E., Goretti, B., Zipoli, V., Hakiki, B., Giannini, M., Pastò, L., and Razzolini, L. (2010). Cognitive impairment in early stages of multiple sclerosis. Neurol Sci *31*, 211–214.

Avramiea, A.-E., Masood, A., Mansvelder, H.D., and Linkenkaer-Hansen, K. (2021). Amplitude and phase coupling optimize information transfer between brain networks that function at criticality. BioRxiv 2021.03.15.435461.

Baillet, S., Mosher, J.C., and Leahy, R.M. (2001). Electromagnetic brain mapping. IEEE Signal Processing Magazine *18*, 14–30.

Basti, A., Pizzella, V., Chella, F., Romani, G.L., Nolte, G., and Marzetti, L. (2018). Disclosing large-scale directed functional connections in MEG with the multivariate phase slope index. NeuroImage *175*, 161–175.

Benedict, R.H.B., and Zivadinov, R. (2011). Risk factors for and management of cognitive dysfunction in multiple sclerosis. Nature Reviews Neurology *7*, 332–342.

Benedict, R.H.B., Weinstock-Guttman, B., Fishman, I., Sharma, J., Tjoa, C.W., and Bakshi, R. (2004). Prediction of Neuropsychological Impairment in Multiple Sclerosis: Comparison of Conventional Magnetic Resonance Imaging Measures of Atrophy and Lesion Burden. Archives of Neurology *61*, 226.

Benjamini, Y., and Hochberg, Y. (1995). Controlling the False Discovery Rate: A Practical and Powerful Approach to Multiple Testing. Journal of the Royal Statistical Society. Series B (Methodological) *57*, 289–300.

Bergholm, F., Adler, J., and Parmryd, I. (2010). Analysis of bias in the apparent correlation coefficient between image pairs corrupted by severe noise. Journal of Mathematical Imaging and Vision *37*, 204–219.

Biswal, B., Yetkin, F.Z., Haughton, V.M., and Hyde, J.S. (1995). Functional connectivity in the motor cortex of resting human brain using echo-planar MRI. Magn Reson Med *34*, 537–541.

Biswal, B.B., Mennes, M., Zuo, X.-N., Gohel, S., Kelly, C., Smith, S.M., Beckmann, C.F., Adelstein, J.S., Buckner, R.L., Colcombe, S., et al. (2010). Toward discovery science of human brain function. Proc. Natl. Acad. Sci. U.S.A. *107*, 4734–4739.

Bosman, C.A., Schoffelen, J.-M., Brunet, N., Oostenveld, R., Bastos, A.M., Womelsdorf, T., Rubehn, B., Stieglitz, T., De Weerd, P., and Fries, P. (2012). Attentional Stimulus Selection through Selective Synchronization between Monkey Visual Areas. Neuron *75*, 875–888.

Boto, E., Hill, R.M., Rea, M., Holmes, N., Seedat, Z.A., Leggett, J., Shah, V., Osborne, J., Bowtell, R., and Brookes, M.J. (2021). Measuring functional connectivity with wearable MEG. NeuroImage 117815.

Brink, R.L. van den, Pfeffer, T., Warren, C.M., Murphy, P.R., Tona, K.-D., Wee, N.J.A. van der, Giltay, E., Noorden, M.S. van, Rombouts, S.A.R.B., Donner, T.H., et al. (2016). Catecholaminergic Neuromodulation Shapes Intrinsic MRI Functional Connectivity in the Human Brain. J. Neurosci. *36*, 7865–7876.

Brink, R.L. van den, Nieuwenhuis, S., and Donner, T.H. (2018). Amplification and Suppression of Distinct Brainwide Activity Patterns by Catecholamines. J. Neurosci. *38*, 7476–7491.

van den Brink, R.L., Pfeffer, T., and Donner, T.H. (2019). Brainstem Modulation of Large-Scale Intrinsic Cortical Activity Correlations. Front. Hum. Neurosci. *13*.

Brookes, M.J., Woolrich, M., Luckhoo, H., Price, D., Hale, J.R., Stephenson, M.C., Barnes, G.R., Smith, S.M., and Morris, P.G. (2011). Investigating the electrophysiological basis of resting state networks using magnetoencephalography. Proc. Natl. Acad. Sci. U.S.A. *108*, 16783–16788.

Brookes, M.J., Woolrich, M.W., and Barnes, G.R. (2012). Measuring functional connectivity in MEG: a multivariate approach insensitive to linear source leakage. Neuroimage *63*, 910–920.

Brookes, M.J., O'Neill, G.C., Hall, E.L., Woolrich, M.W., Baker, A., Palazzo Corner, S., Robson, S.E., Morris, P.G., and Barnes, G.R. (2014). Measuring temporal, spectral and spatial changes in electrophysiological brain network connectivity. Neuroimage *91*, 282–299.

Bruns, A., Eckhorn, R., Jokeit, H., and Ebner, A. (2000). Amplitude envelope correlation detects coupling among incoherent brain signals. Neuroreport *11*, 1509–1514.

Burns, S.P., Santaniello, S., Yaffe, R.B., Jouny, C.C., Crone, N.E., Bergey, G.K., Anderson, W.S., and Sarma, S.V. (2014). Network dynamics of the brain and influence of the epileptic seizure onset zone. PNAS *111*, E5321–E5330.

Buschman, T.J., and Miller, E.K. (2007). Top-Down Versus Bottom-Up Control of Attention in the Prefrontal and Posterior Parietal Cortices. Science *315*, 1860–1862.

Buschman, T.J., Denovellis, E.L., Diogo, C., Bullock, D., and Miller, E.K. (2012). Synchronous Oscillatory Neural Ensembles for Rules in the Prefrontal Cortex. Neuron *76*, 838–846.

Cetin, M.S., Houck, J.M., Rashid, B., Agacoglu, O., Stephen, J.M., Sui, J., Canive, J., Mayer, A., Aine, C., Bustillo, J.R., et al. (2016). Multimodal Classification of Schizophrenia Patients with MEG and fMRI Data Using Static and Dynamic Connectivity Measures. Front Neurosci *10*.

Chaumon, M., Bishop, D.V.M., and Busch, N.A. (2015). A practical guide to the selection of independent components of the electroencephalogram for artifact correction. J. Neurosci. Methods *250*, 47–63.

Chiaravalloti, N.D., and DeLuca, J. (2008). Cognitive impairment in multiple sclerosis. The Lancet Neurology *7*, 1139–1151.

Cogliati Dezza, I., Zito, G., Tomasevic, L., Filippi, M.M., Ghazaryan, A., Porcaro, C., Squitti, R., Ventriglia, M., Lupoi, D., and Tecchio, F. (2015). Functional and structural balances of homologous sensorimotor regions in multiple sclerosis fatigue. J. Neurol. *262*, 614–622.

Colclough, G.L., Brookes, M.J., Smith, S.M., and Woolrich, M.W. (2015). A symmetric multivariate leakage correction for MEG connectomes. Neuroimage *117*, 439–448.

Colclough, G.L., Woolrich, M.W., Tewarie, P.K., Brookes, M.J., Quinn, A.J., and Smith, S.M. (2016). How reliable are MEG resting-state connectivity metrics? Neuroimage *138*, 284–293.

Cover, K.S., Vrenken, H., Geurts, J.J.G., van Oosten, B.W., Jelles, B., Polman, C.H., Stam, C.J., and van Dijk, B.W. (2006a). Multiple sclerosis patients show a highly significant decrease in alpha band interhemispheric synchronization measured using MEG. NeuroImage *29*, 783–788.

Cover, K.S., Vrenken, H., Geurts, J.J.G., van Oosten, B.W., Jelles, B., Polman, C.H., Stam, C.J., and van Dijk, B.W. (2006b). Multiple sclerosis patients show a highly significant decrease in alpha band interhemispheric synchronization measured using MEG. Neuroimage *29*, 783–788.

Crossley, N.A., Mechelli, A., Scott, J., Carletti, F., Fox, P.T., McGuire, P., and Bullmore, E.T. (2014). The hubs of the human connectome are generally implicated in the anatomy of brain disorders. Brain *137*, 2382–2395.

Daffertshofer, A., Ton, R., Kringelbach, M.L., Woolrich, M., and Deco, G. (2018). Distinct criticality of phase and amplitude dynamics in the resting brain. NeuroImage *180*, 442–447.

Deco, G., and Corbetta, M. (2011). The dynamical balance of the brain at rest. Neuroscientist *17*, 107–123.

Dehaene, S., and Changeux, J.-P. (2011). Experimental and Theoretical Approaches to Conscious Processing. Neuron *70*, 200–227.

van Dellen, E., van der Kooi, A.W., Numan, T., Koek, H.L., Klijn, F.A.M., Buijsrogge, M.P., Stam, C.J., and Slooter, A.J.C. (2014). Decreased functional connectivity and disturbed directionality of information flow in the electroencephalography of intensive care unit patients with delirium after cardiac surgery. Anesthesiology *121*, 328–335.

Dendrou, C.A., Fugger, L., and Friese, M.A. (2015). Immunopathology of multiple sclerosis. Nature Reviews Immunology *15*, 545–558.

Destexhe, A., Contreras, D., and Steriade, M. (1999). Spatiotemporal analysis of local field potentials and unit discharges in cat cerebral cortex during natural wake and sleep states. J. Neurosci. *19*, 4595–4608.

van Diessen, E., Numan, T., van Dellen, E., van der Kooi, A.W., Boersma, M., Hofman, D., van Lutterveld, R., van Dijk, B.W., van Straaten, E.C.W., Hillebrand, A., et

al. (2015). Opportunities and methodological challenges in EEG and MEG resting state functional brain network research. Clin Neurophysiol *126*, 1468–1481.

Donner, T.H., and Siegel, M. (2011a). A framework for local cortical oscillation patterns. Trends in Cognitive Sciences *15*, 191–199.

Donner, T.H., and Siegel, M. (2011b). A framework for local cortical oscillation patterns. Trends Cogn Sci *15*, 191–199.

Engel, A.K., Fries, P., and Singer, W. (2001). Dynamic predictions: oscillations and synchrony in top-down processing. Nat. Rev. Neurosci. *2*, 704–716.

Engel, A.K., Gerloff, C., Hilgetag, C.C., and Nolte, G. (2013). Intrinsic coupling modes: multiscale interactions in ongoing brain activity. Neuron *80*, 867–886.

Fell, J., and Axmacher, N. (2011). The role of phase synchronization in memory processes. Nat Rev Neurosci *12*, 105–118.

Figueroa-Vargas, A., Cárcamo, C., Henríquez-Ch, R., Zamorano, F., Ciampi, E., Uribe-San-Martin, R., Vásquez, M., Aboitiz, F., and Billeke, P. (2020). Frontoparietal connectivity correlates with working memory performance in multiple sclerosis. Scientific Reports *10*, 9310.

Fischer, J.S., Rudick, R.A., Cutter, G.R., and Reingold, S.C. (1999). The Multiple Sclerosis Functional Composite measure (MSFC): an integrated approach to MS clinical outcome assessment. Mult Scler *5*, 244–250.

Fornito, A., Zalesky, A., and Breakspear, M. (2015). The connectomics of brain disorders. Nat. Rev. Neurosci. *16*, 159–172.

Fox, M.D., and Raichle, M.E. (2007). Spontaneous fluctuations in brain activity observed with functional magnetic resonance imaging. Nat. Rev. Neurosci. *8*, 700–711.

Fries, P. (2005). A mechanism for cognitive dynamics: neuronal communication through neuronal coherence. Trends Cogn Sci *9*, 474–480.

Fries, P. (2015). Rhythms for Cognition: Communication through Coherence. Neuron *88*, 220–235.

Friston, K.J. (1994). Functional and effective connectivity in neuroimaging: A synthesis. Human Brain Mapping *2*, 56–78.

Froemke, R.C. (2015). Plasticity of Cortical Excitatory-Inhibitory Balance. Annual Review of Neuroscience *38*, 195–219.

Geschwind, N. (1970). The Organization of Language and the Brain. Science *170*, 940–944.

Geschwind, N. (1979). Specializations of the Human Brain. Scientific American *241*, 180–201.

Goupillaud, P., Grossmann, A., and Morlet, J. (1984). Cycle-octave and related transforms in seismic signal analysis. Geoexploration *23*, 85–102.

Gross, J., Kujala, J., Hamalainen, M., Timmermann, L., Schnitzler, A., and Salmelin, R. (2001). Dynamic imaging of coherent sources: Studying neural interactions in the human brain. Proc. Natl. Acad. Sci. U.S.A. *98*, 694–699.

Gschwind, M., Hardmeier, M., Van De Ville, D., Tomescu, M.I., Penner, I.-K., Naegelin, Y., Fuhr, P., Michel, C.M., and Seeck, M. (2016). Fluctuations of spontaneous EEG topographies predict disease state in relapsing-remitting multiple sclerosis. Neuroimage Clin *12*, 466–477.

Hardmeier, M., Schoonheim, M.M., Geurts, J.J.G., Hillebrand, A., Polman, C.H., Barkhof, F., and Stam, C.J. (2012). Cognitive dysfunction in early multiple sclerosis: altered centrality derived from resting-state functional connectivity using magneto-encephalography. PLoS ONE *7*, e42087.

Hawellek, D.J., Hipp, J.F., Lewis, C.M., Corbetta, M., and Engel, A.K. (2011). Increased functional connectivity indicates the severity of cognitive impairment in multiple sclerosis. PNAS *108*, 19066–19071.

Hawellek, D.J., Schepers, I.M., Roeder, B., Engel, A.K., Siegel, M., and Hipp, J.F. (2013). Altered intrinsic neuronal interactions in the visual cortex of the blind. J. Neurosci. *33*, 17072–17080.

Helekar, S.A., Shin, J., Mattson, B.J., Bartley, K., Stosic, M., Saldana-King, T., Montague, R., and Hutton, G.J. (2010). Functional Brain Network Changes Associated with Maintenance of Cognitive Function in Multiple Sclerosis. Front. Hum. Neurosci. *4*.

Herculano-Houzel, S. (2009). The human brain in numbers: a linearly scaled-up primate brain. Front. Hum. Neurosci. *3*.

Heuvel, M.P. van den, and Sporns, O. (2019). A cross-disorder connectome landscape of brain dysconnectivity. Nat Rev Neurosci *20*, 435–446.

Hillebrand, A., Barnes, G.R., Bosboom, J.L., Berendse, H.W., and Stam, C.J. (2012). Frequency-dependent functional connectivity within resting-state networks: an atlas-based MEG beamformer solution. Neuroimage *59*, 3909–3921.

Hipp, J.F., and Siegel, M. (2013). Dissociating neuronal gamma-band activity from cranial and ocular muscle activity in EEG. Front Hum Neurosci *7*, 338.

Hipp, J.F., and Siegel, M. (2015). BOLD fMRI Correlation Reflects Frequency-Specific Neuronal Correlation. Curr. Biol. *25*, 1368–1374.

Hipp, J.F., Engel, A.K., and Siegel, M. (2011a). Oscillatory synchronization in large-scale cortical networks predicts perception. Neuron *69*, 387–396.

Hipp, J.F., Engel, A.K., and Siegel, M. (2011b). Oscillatory synchronization in large-scale cortical networks predicts perception. Neuron *69*, 387–396.

Hipp, J.F., Hawellek, D.J., Corbetta, M., Siegel, M., and Engel, A.K. (2012). Large-scale cortical correlation structure of spontaneous oscillatory activity. Nat. Neurosci. *15*, 884–890.

Hyvärinen, A., and Oja, E. (2000). Independent component analysis: algorithms and applications. Neural Netw *13*, 411–430.

Jahnke, S., Memmesheimer, R.-M., and Timme, M. (2014). Oscillation-induced signal transmission and gating in neural circuits. PLoS Comput. Biol. *10*, e1003940.

Jensen, O., and Mazaheri, A. (2010). Shaping functional architecture by oscillatory alpha activity: gating by inhibition. Front Hum Neurosci *4*, 186.

Kandel, E.R., Schwartz, J.H., Jessell, T.M., Biochemistry, D. of, Jessell, M.B.T., Siegelbaum, S., and Hudspeth, A.J. (2000). Principles of neural science (McGraw-hill New York).

Kitzbichler, M.G., Khan, S., Ganesan, S., Vangel, M.G., Herbert, M.R., Hämäläinen, M.S., and Kenet, T. (2015). Altered development and multifaceted band-specific abnormalities of resting state networks in autism. Biol. Psychiatry *77*, 794–804.

Kocevar, G., Stamile, C., Hannoun, S., Cotton, F., Vukusic, S., Durand-Dubief, F., and Sappey-Marinier, D. (2016). Graph Theory-Based Brain Connectivity for Automatic Classification of Multiple Sclerosis Clinical Courses. Front. Neurosci. *10*.

Koelewijn, L., Bompas, A., Tales, A., Brookes, M.J., Muthukumaraswamy, S.D., Bayer, A., and Singh, K.D. (2017). Alzheimer's disease disrupts alpha and beta-band resting-state oscillatory network connectivity. Clinical Neurophysiology.

Krishnan, G.P., González, O.C., and Bazhenov, M. (2018). Origin of slow spontaneous resting-state neuronal fluctuations in brain networks. Proc. Natl. Acad. Sci. U.S.A.

Kurtzke, J.F. (1983). Rating neurologic impairment in multiple sclerosis. Neurology *33*, 1444.

Landau, A.N., and Fries, P. (2012). Attention samples stimuli rhythmically. Curr. Biol. *22*, 1000–1004.

Landau, A.N., Schreyer, H.M., van Pelt, S., and Fries, P. (2015). Distributed Attention Is Implemented through Theta-Rhythmic Gamma Modulation. Curr. Biol. *25*, 2332–2337.

Larson-Prior, L.J., Power, J.D., Vincent, J.L., Nolan, T.S., Coalson, R.S., Zempel, J., Snyder, A.Z., Schlaggar, B.L., Raichle, M.E., and Petersen, S.E. (2011). Modulation of the brain's functional network architecture in the transition from wake to sleep. Prog. Brain Res. *193*, 277–294.

Larson-Prior, L.J., Oostenveld, R., Della Penna, S., Michalareas, G., Prior, F., Babajani-Feremi, A., Schoffelen, J.-M., Marzetti, L., de Pasquale, F., Di Pompeo, F., et al. (2013). Adding dynamics to the Human Connectome Project with MEG. NeuroImage *80*, 190–201.

Leopold, D.A., Murayama, Y., and Logothetis, N.K. (2003). Very slow activity fluctuations in monkey visual cortex: implications for functional brain imaging. Cereb. Cortex *13*, 422–433.

Liu, Y., Wang, H., Duan, Y., Huang, J., Ren, Z., Ye, J., Dong, H., Shi, F., Li, K., and Wang, J. (2016). Functional Brain Network Alterations in Clinically Isolated Syndrome and Multiple Sclerosis: A Graph-based Connectome Study. Radiology *282*, 534–541.

Logothetis, N.K. (2008). What we can do and what we cannot do with fMRI. Nature *453*, 869–878.

Lopes da Silva, F. (2013). EEG and MEG: relevance to neuroscience. Neuron *80*, 1112–1128.

Lublin, F.D., and Reingold, S.C. (1996). Defining the clinical course of multiple sclerosis. Neurology *46*, 907.

Maestú, F., Peña, J.-M., Garcés, P., González, S., Bajo, R., Bagic, A., Cuesta, P., Funke, M., Mäkelä, J.P., Menasalvas, E., et al. (2015). A multicenter study of the early detection of synaptic dysfunction in Mild Cognitive Impairment using Magnetoencephalography-derived functional connectivity. NeuroImage: Clinical *9*, 103–109.

Mantini, D., Perrucci, M.G., Del Gratta, C., Romani, G.L., and Corbetta, M. (2007). Electrophysiological signatures of resting state networks in the human brain. Proc. Natl. Acad. Sci. U.S.A. *104*, 13170–13175.

Mantini, D., Penna, S.D., Marzetti, L., de Pasquale, F., Pizzella, V., Corbetta, M., and Romani, G.L. (2011). A Signal-Processing Pipeline for Magnetoencephalography Resting-State Networks. Brain Connectivity *1*, 49–59.

Maran, M., Grent-'t-Jong, T., and Uhlhaas, P.J. (2016). Electrophysiological insights into connectivity anomalies in schizophrenia: a systematic review. Neuropsychiatric Electrophysiology *2*, 6.

Marzetti, L., Basti, A., Chella, F., D'Andrea, A., Syrjälä, J., and Pizzella, V. (2019). Brain Functional Connectivity Through Phase Coupling of Neuronal Oscillations: A Perspective From Magnetoencephalography. Front Neurosci *13*.

Mehrkanoon, S., Breakspear, M., Britz, J., and Boonstra, T.W. (2014). Intrinsic coupling modes in source-reconstructed electroencephalography. Brain Connect *4*, 812–825.

Murphy, B.K., and Miller, K.D. (2003). Multiplicative Gain Changes Are Induced by Excitation or Inhibition Alone. J. Neurosci. *23*, 10040–10051.

von Nicolai, C., Engler, G., Sharott, A., Engel, A.K., Moll, C.K., and Siegel, M. (2014). Corticostriatal coordination through coherent phase-amplitude coupling. J. Neurosci. *34*, 5938–5948.

Nir, Y., Mukamel, R., Dinstein, I., Privman, E., Harel, M., Fisch, L., Gelbard-Sagiv, H., Kipervasser, S., Andelman, F., Neufeld, M.Y., et al. (2008). Interhemispheric correlations of slow spontaneous neuronal fluctuations revealed in human sensory cortex. Nat. Neurosci. *11*, 1100–1108.

Nolte, G. (2003). The magnetic lead field theorem in the quasi-static approximation and its use for magnetoencephalography forward calculation in realistic volume conductors. Phys. Med. Biol. *48*, 3637.

Nolte, G., Bai, O., Wheaton, L., Mari, Z., Vorbach, S., and Hallett, M. (2004). Identifying true brain interaction from EEG data using the imaginary part of coherency. Clin Neurophysiol *115*, 2292–2307.

Nolte, G., Galindo-Leon, E., Li, Z., Liu, X., and Engel, A.K. (2020). Mathematical Relations Between Measures of Brain Connectivity Estimated From Electrophysiological Recordings for Gaussian Distributed Data. Front Neurosci *14*, 577574.

O'Neill, G.C., Bauer, M., Woolrich, M.W., Morris, P.G., Barnes, G.R., and Brookes, M.J. (2015). Dynamic recruitment of resting state sub-networks. NeuroImage *115*, 85–95.

Oostenveld, R., Fries, P., Maris, E., and Schoffelen, J.-M. (2010). FieldTrip: Open Source Software for Advanced Analysis of MEG, EEG, and Invasive Electrophysiological Data. Computational Intelligence and Neuroscience *2011*, e156869.

Oswal, A., Beudel, M., Zrinzo, L., Limousin, P., Hariz, M., Foltynie, T., Litvak, V., and Brown, P. (2016). Deep brain stimulation modulates synchrony within spatially and spectrally distinct resting state networks in Parkinson's disease. Brain *139*, 1482–1496.

Palva, J.M., Monto, S., Kulashekhar, S., and Palva, S. (2010a). Neuronal synchrony reveals working memory networks and predicts individual memory capacity. PNAS *107*, 7580–7585.

Palva, J.M., Wang, S.H., Palva, S., Zhigalov, A., Monto, S., Brookes, M.J., Schoffelen, J.-M., and Jerbi, K. (2018). Ghost interactions in MEG/EEG source space: A note of caution on inter-areal coupling measures. Neuroimage *173*, 632–643.

Palva, S., Monto, S., and Palva, J.M. (2010b). Graph properties of synchronized cortical networks during visual working memory maintenance. NeuroImage *49*, 3257–3268.

Pappu, V., and Pardalos, P.M. (2014). High-Dimensional Data Classification. In Clusters, Orders, and Trees: Methods and Applications: In Honor of Boris Mirkin's 70th Birthday, F. Aleskerov, B. Goldengorin, and P.M. Pardalos, eds. (New York, NY: Springer), pp. 119–150.

Pascual-Marqui, R.D. (2007). Instantaneous and lagged measurements of linear and nonlinear dependence between groups of multivariate time series: frequency decomposition. ArXiv:0711.1455 [Stat].

Pascual-Marqui, R.D., Esslen, M., Kochi, K., and Lehmann, D. (2002). Functional imaging with low resolution brain electromagnetic tomography (LORETA): review, new comparisons, and new validation. 19.

Pascual-Marqui, R.D., Lehmann, D., Koukkou, M., Kochi, K., Anderer, P., Saletu, B., Tanaka, H., Hirata, K., John, E.R., Prichep, L., et al. (2011). Assessing interactions in the brain with exact low-resolution electromagnetic tomography. Philosophical Transactions of the Royal Society A: Mathematical, Physical and Engineering Sciences *369*, 3768–3784.

Pesaran, B., Vinck, M., Einevoll, G.T., Sirota, A., Fries, P., Siegel, M., Truccolo, W., Schroeder, C.E., and Srinivasan, R. (2018). Investigating large-scale brain dynamics

using field potential recordings: analysis and interpretation. Nature Neuroscience *21*, 903–919.

Pfeffer, T., Avramiea, A.-E., Nolte, G., Engel, A.K., Linkenkaer-Hansen, K., and Donner, T.H. (2018). Catecholamines alter the intrinsic variability of cortical population activity and perception. PLOS Biology *16*, e2003453.

Pfeffer, T., Ponce-Alvarez, A., Meindertsma, T., Gahnström, C., Brink, R.L. van den, Nolte, G., Tsetsos, K., Engel, A.K., Deco, G., and Donner, T.H. (2020). Circuit mechanisms for chemical modulation of cortex-wide network interactions and exploration behavior. BioRxiv 2020.06.25.171199.

Poeppel, D., Emmorey, K., Hickok, G., and Pylkkänen, L. (2012). Towards a New Neurobiology of Language. J. Neurosci. *32*, 14125–14131.

Polack, P.-O., Friedman, J., and Golshani, P. (2013). Cellular mechanisms of brain state–dependent gain modulation in visual cortex. Nat Neurosci *16*, 1331–1339.

Polman, C.H., Reingold, S.C., Banwell, B., Clanet, M., Cohen, J.A., Filippi, M., Fujihara, K., Havrdova, E., Hutchinson, M., Kappos, L., et al. (2011). Diagnostic criteria for multiple sclerosis: 2010 Revisions to the McDonald criteria. Annals of Neurology *69*, 292–302.

Quinn, A.J., van Ede, F., Brookes, M.J., Heideman, S.G., Nowak, M., Seedat, Z.A., Vidaurre, D., Zich, C., Nobre, A.C., and Woolrich, M.W. (2019). Unpacking Transient Event Dynamics in Electrophysiological Power Spectra. Brain Topogr *32*, 1020–1034.

Raichle, M.E. (2015). The Brain's Default Mode Network. Annual Review of Neuroscience *38*, 433–447.

Raichle, M.E., MacLeod, A.M., Snyder, A.Z., Powers, W.J., Gusnard, D.A., and Shulman, G.L. (2001). A default mode of brain function. Proc. Natl. Acad. Sci. U.S.A. *98*, 676–682.

Rocca, M.A., Valsasina, P., Martinelli, V., Misci, P., Falini, A., Comi, G., and Filippi, M. (2012). Large-scale neuronal network dysfunction in relapsing-remitting multiple sclerosis. Neurology *79*, 1449–1457.

Roosendaal, S.D., Geurts, J.J.G., Vrenken, H., Hulst, H.E., Cover, K.S., Castelijns, J.A., Pouwels, P.J.W., and Barkhof, F. (2009). Regional DTI differences in multiple sclerosis patients. NeuroImage *44*, 1397–1403.

Rubinov, M., and Sporns, O. (2010). Complex network measures of brain connectivity: uses and interpretations. Neuroimage *52*, 1059–1069.

Schneider, M., Dann, B., Sheshadri, S., Scherberger, H., and Vinck, M. (2020). A general theory of coherence between brain areas. BioRxiv 2020.06.17.156190.

Schoonheim, M.M., Geurts, J.J.G., Landi, D., Douw, L., van der Meer, M.L., Vrenken, H., Polman, C.H., Barkhof, F., and Stam, C.J. (2013). Functional connectivity changes in multiple sclerosis patients: A graph analytical study of MEG resting state data. Hum. Brain Mapp. *34*, 52–61.

Schoonheim, M.M., Meijer, K.A., and Geurts, J.J.G. (2015). Network Collapse and Cognitive Impairment in Multiple Sclerosis. Front Neurol *6*.

Schoonhoven, D.N., Fraschini, M., Tewarie, P., Uitdehaag, B.M., Eijlers, A.J., Geurts, J.J., Hillebrand, A., Schoonheim, M.M., Stam, C.J., and Strijbis, E.M. (2019). Resting-state MEG measurement of functional activation as a biomarker for cognitive decline in MS. Mult Scler *25*, 1896–1906.

Shine, J.M., van den Brink, R.L., Hernaus, D., Nieuwenhuis, S., and Poldrack, R.A. (2018). Catecholaminergic manipulation alters dynamic network topology across cognitive states. Network Neuroscience *2*, 381–396.

Shu, N., Liu, Y., Li, K., Duan, Y., Wang, J., Yu, C., Dong, H., Ye, J., and He, Y. (2011). Diffusion Tensor Tractography Reveals Disrupted Topological Efficiency in White Matter Structural Networks in Multiple Sclerosis. Cereb Cortex *21*, 2565–2577.

Siegel, M., Donner, T.H., Oostenveld, R., Fries, P., and Engel, A.K. (2008). Neuronal synchronization along the dorsal visual pathway reflects the focus of spatial attention. Neuron *60*, 709–719.

Siegel, M., Donner, T.H., and Engel, A.K. (2012). Spectral fingerprints of large-scale neuronal interactions. Nat. Rev. Neurosci. *13*, 121–134.

Siems, M., and Siegel, M. (2020). Dissociated neuronal phase- and amplitude-coupling patterns in the human brain. NeuroImage 116538.

Siems, M., Pape, A.-A., Hipp, J.F., and Siegel, M. (2016). Measuring the cortical correlation structure of spontaneous oscillatory activity with EEG and MEG. Neuroimage *129*, 345–355.

Siems, M., Tünnerhoff, J., Ziemann, U., and Siegel, M. (2021). Altered cortical phase- and amplitude-coupling in Multiple Sclerosis. BioRxiv 2021.02.17.431597.

Singer, W. (1999). Neuronal Synchrony: A Versatile Code for the Definition of Relations? Neuron *24*, 49–65.

Singer, W. (2013). Cortical dynamics revisited. Trends in Cognitive Sciences *17*, 616–626.

Sjøgård, M., Wens, V., Schependom, J.V., Costers, L., D'hooghe, M., D'haeseleer, M., Woolrich, M., Goldman, S., Nagels, G., and Tiège, X.D. (2021). Brain dysconnectivity relates to disability and cognitive impairment in multiple sclerosis. Human Brain Mapping *42*, 626–643.

Smith, S.M., Fox, P.T., Miller, K.L., Glahn, D.C., Fox, P.M., Mackay, C.E., Filippini, N., Watkins, K.E., Toro, R., Laird, A.R., et al. (2009). Correspondence of the brain's functional architecture during activation and rest. Proc. Natl. Acad. Sci. U.S.A. *106*, 13040–13045.

Snyder, A.C., Issar, D., and Smith, M.A. (2018). What does scalp electroencephalogram coherence tell us about long-range cortical networks? European Journal of Neuroscience *48*, 2466–2481.

Spearman, C. (1904). The proof and measurement of association between two things. The American Journal of Psychology *15*, 72–101.

Stam, C.J. (2014). Modern network science of neurological disorders. Nat. Rev. Neurosci. *15*, 683–695.

Stam, C.J., Nolte, G., and Daffertshofer, A. (2007). Phase lag index: Assessment of functional connectivity from multi channel EEG and MEG with diminished bias from common sources. Human Brain Mapping *28*, 1178–1193.

Tewarie, P., Schoonheim, M.M., Stam, C.J., van der Meer, M.L., van Dijk, B.W., Barkhof, F., Polman, C.H., and Hillebrand, A. (2013). Cognitive and Clinical Dysfunction, Altered MEG Resting-State Networks and Thalamic Atrophy in Multiple Sclerosis. PLoS ONE *8*, e69318.

Tewarie, P., Steenwijk, M.D., Tijms, B.M., Daams, M., Balk, L.J., Stam, C.J., Uitdehaag, B.M.J., Polman, C.H., Geurts, J.J.G., Barkhof, F., et al. (2014a). Disruption of structural and functional networks in long-standing multiple sclerosis. Hum Brain Mapp *35*, 5946–5961.

Tewarie, P., Hillebrand, A., Schoonheim, M.M., van Dijk, B.W., Geurts, J.J.G., Barkhof, F., Polman, C.H., and Stam, C.J. (2014b). Functional brain network analysis using minimum spanning trees in Multiple Sclerosis: An MEG source-space study. NeuroImage *88*, 308–318.

Tewarie, P., Hunt, B.A.E., O'Neill, G.C., Byrne, A., Aquino, K., Bauer, M., Mullinger, K.J., Coombes, S., and Brookes, M.J. (2018a). Relationships Between Neuronal Oscillatory Amplitude and Dynamic Functional Connectivity. Cereb. Cortex.

Tewarie, P., Steenwijk, M.D., Brookes, M.J., Uitdehaag, B.M.J., Geurts, J.J.G., Stam, C.J., and Schoonheim, M.M. (2018b). Explaining the heterogeneity of functional connectivity findings in multiple sclerosis: An empirically informed modeling study. Human Brain Mapping *39*, 2541–2548.

Tin Kam Ho (1998). The random subspace method for constructing decision forests. IEEE Transactions on Pattern Analysis and Machine Intelligence *20*, 832–844.

Van Essen, D.C., Smith, S.M., Barch, D.M., Behrens, T.E.J., Yacoub, E., and Ugurbil, K. (2013). The WU-Minn Human Connectome Project: An overview. NeuroImage *80*, 62–79.

Van Schependom, J., Gielen, J., Laton, J., D'hooghe, M.B., De Keyser, J., and Nagels, G. (2014a). Graph theoretical analysis indicates cognitive impairment in MS stems from neural disconnection. NeuroImage: Clinical *4*, 403–410.

Van Schependom, J., Gielen, J., Laton, J., D'hooghe, M.B., De Keyser, J., and Nagels, G. (2014b). Graph theoretical analysis indicates cognitive impairment in MS stems from neural disconnection. NeuroImage: Clinical *4*, 403–410.

Van Veen, B.D., van Drongelen, W., Yuchtman, M., and Suzuki, A. (1997). Localization of brain electrical activity via linearly constrained minimum variance spatial filtering. IEEE Trans Biomed Eng *44*, 867–880.

Vidaurre, D., Smith, S.M., and Woolrich, M.W. (2017). Brain network dynamics are hierarchically organized in time. Proc Natl Acad Sci USA *114*, 12827–12832.

Vidaurre, D., Abeysuriya, R., Becker, R., Quinn, A.J., Alfaro-Almagro, F., Smith, S.M., and Woolrich, M.W. (2018). Discovering dynamic brain networks from big data in rest and task. NeuroImage *180*, 646–656.

Vinck, M., Oostenveld, R., van Wingerden, M., Battaglia, F., and Pennartz, C.M.A. (2011). An improved index of phase-synchronization for electrophysiological data in the presence of volume-conduction, noise and sample-size bias. NeuroImage *55*, 1548–1565.

Voytek, B., and Knight, R.T. (2015). Dynamic network communication as a unifying neural basis for cognition, development, aging, and disease. Biol. Psychiatry *77*, 1089–1097.

Wang, H.E., Bénar, C.G., Quilichini, P.P., Friston, K.J., Jirsa, V.K., and Bernard, C. (2014). A systematic framework for functional connectivity measures. Front. Neurosci *8*, 405.

Wang, S.H., Lobier, M., Siebenhühner, F., Puoliväli, T., Palva, S., and Palva, J.M. (2018). Hyperedge bundling: A practical solution to spurious interactions in MEG/EEG source connectivity analyses. Neuroimage *173*, 610–622.

Wens, V., Bourguignon, M., Goldman, S., Marty, B., Op de Beeck, M., Clumeck, C., Mary, A., Peigneux, P., Van Bogaert, P., Brookes, M.J., et al. (2014). Inter- and intra-subject variability of neuromagnetic resting state networks. Brain Topogr *27*, 620–634.

Wens, V., Marty, B., Mary, A., Bourguignon, M., Beeck, M.O. de, Goldman, S., Bogaert, P.V., Peigneux, P., and Tiège, X.D. (2015). A geometric correction scheme for spatial leakage effects in MEG/EEG seed-based functional connectivity mapping. Human Brain Mapping *36*, 4604–4621.

Wernicke, C. (1874). Der aphasische Symptomencomplex: Eine psychologische Studie auf anatomischer Basis (Cohn.).

Womelsdorf, T., Schoffelen, J.-M., Oostenveld, R., Singer, W., Desimone, R., Engel, A.K., and Fries, P. (2007). Modulation of Neuronal Interactions Through Neuronal Synchronization. Science *316*, 1609–1612.

Yeo, B.T.T., Krienen, F.M., Sepulcre, J., Sabuncu, M.R., Lashkari, D., Hollinshead, M., Roffman, J.L., Smoller, J.W., Zöllei, L., Polimeni, J.R., et al. (2011). The organization of the human cerebral cortex estimated by intrinsic functional connectivity. J. Neurophysiol. *106*, 1125–1165.

Zerouali, Y., Pouliot, P., Robert, M., Mohamed, I., Bouthillier, A., Lesage, F., and Nguyen, D.K. (2016). Magnetoencephalographic signatures of insular epileptic spikes based on functional connectivity. Hum. Brain Mapp. *37*, 3250–3261.

Zhang, D., and Raichle, M.E. (2010). Disease and the brain's dark energy. Nat Rev Neurol *6*, 15–28.

Zhigalov, A., Arnulfo, G., Nobili, L., Palva, S., and Palva, J.M. (2017). Modular co-organization of functional connectivity and scale-free dynamics in the human brain. Network Neuroscience *1*, 143–165.

8 Acknowledgements

This dissertation is not only me alone working on projects and writing a report but many people alongside me, with everyone contributing in their one unique ways.

First and foremost I'd like to thank my Advisory Board, Christoph Braun & Gabriele Lohman, for keeping an eye out for the studies presented here, giving helpful advice and joining me through all the stages of my doctoral studies.

A special thank you belongs to my doctoral father and supervisor of the last 7 years, Markus Siegel. He introduced me to the world of cutting edge neuroscientific research and has shown me many times that it was a very good decision to stay in Tübingen. Thank you for accompanying me through the cloud to whatever outcome was on the other side.

The infrastructure in Tübingen was great in supporting me as a young, clueless researcher. The International Max-Planck Research School and the Graduate Training Center with their tireless staff has always been helpful and made it possible for me to focus mainly on my studies. Thank you!

A huge part of the presented work wouldn't have been possible, if not for the excellent work of my collaborators in the Neurology Department of the Universitätsklinikum Tübingen. With the help of Johannes Tuennerhoff, Hannah Kramer and Yeo Kim, under the guidance of Prof. Ulf Ziemann, I was able to acquire valuable patient data and compare healthy and diseased brain connectivity.

Successful data acquisition is the cornerstone of good empirical research. I'd therefore like to thank all the people at the MEG Center in Tübingen keeping our facilities up and running, especially Timmo Larbig, Jürgen Dax and Christoph Braun.

Additionally, a big thank you goes to Gabi Walker-Dietrich for sitting with me through countless MEG-sessions and introducing me to our MEG system.

Doing the work is one part, but being a researcher means so much more and the people in the Siegellab have taught me so over the years. Diversity of characters define our lab as an ecosystem. It's when everyone can bring their unique abilities to the table that the entirety of people can blossom. Thank you Siegulls, thank you Joerg Hipp, Constantin von Nicolai, Nima Noury, Florian Sandhaeger, Anna-Antonia Pape, Andrea Ibarra Chaoul, Janet Giehl, Jan Schluesener, Quinglin Li, Angela Radetz, Paul Hege, Malav Shah, David Hawellek, Caterina Trainito and Franziska Pellegrini.

A special thank you goes to Constantin and Nima for their helpful comments on this thesis, Andrea, Constantin and Anna-Antonia for the - sometimes very necessary - emotional support and Joerg for his groundbreaking research that paved the way for so many of my own discoveries.

I wouldn't be here, or anywhere for that matter, if it wouldn't have been for my parents. They always nurtured and supported me and not once in 11 years asked me when I'll finally finish studying and get a "real" job. I love you for what you have done for me. I always dreamt big but only because you showed me how.

Doing research is tough and asks you to make a lot of compromises outside the lab. I'm lucky enough to have found the woman on my side, who does not only understand what I have to do but pushes me even further, beyond what I expect of myself. You always even out my inner scale. My wife, my love, my companion.

Appendix

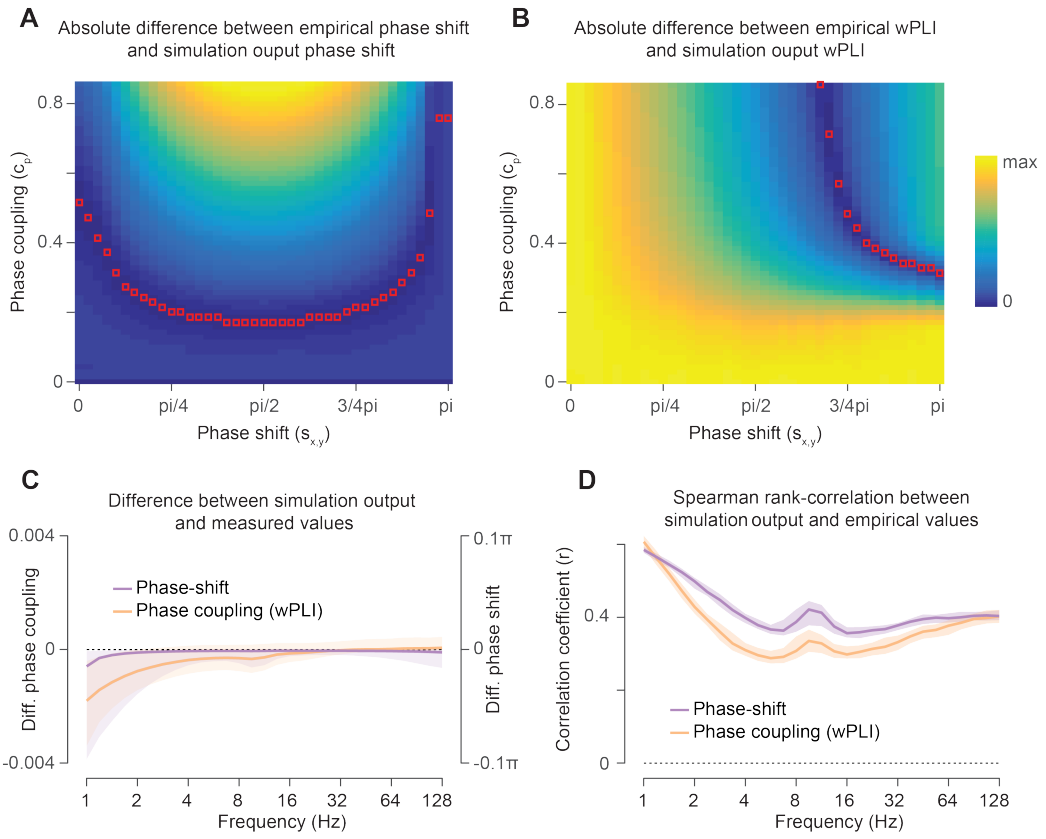

Figure A1. Assessment of parameter estimation

Example distribution (at measured signal mixing of 0.2) of the difference between simulation output and empirically measured (**A**) phase-shift and (**B**) phase coupling as a function of simulation input (x-axis phase-shift, y-axis phase coupling parameter). Red squares indicate the zero contour-line of the minimum difference between simulation output and empirically measured values as a function of input phase-shift and phase-coupling. We chose the intersection between these isolines as the estimated empirical phase shift and phase coupling for the signal construction to obtain simulation outputs with the measured wPLI and phase shift. (**C**) Difference between the optimal simulation output and the empirically measured values. Shaded areas indicate the 5-95% interquantile range across subjects and connection space. (**D**) Rank correlation between the optimal simulation output and the empirically measured values. Shaded areas indicate the 25-75% interquartile range.

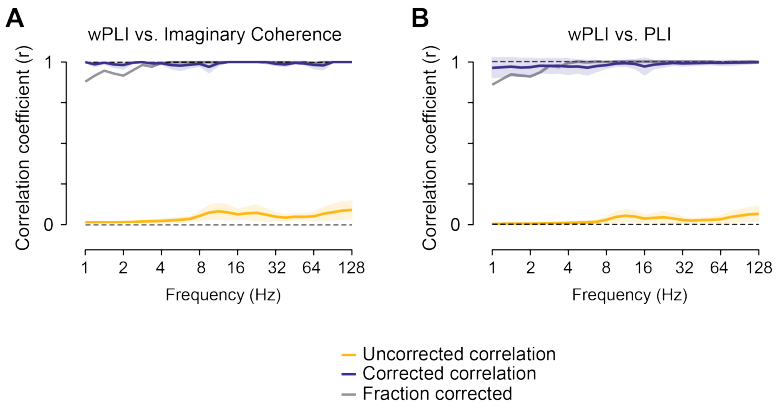

Figure A2. Comparison between phase-coupling measures

Distribution of attenuation corrected (blue) and uncorrected (yellow) correlation between seed-patterns of the weighted phase lag index (wPLI) and imaginary coherency (ImC) (**A**) and of the wPLI and phase lag index (PLI) (**B**). The gray line indicates the relative number of corrected seed patterns. Shaded areas indicate the standard deviation across cortical space.

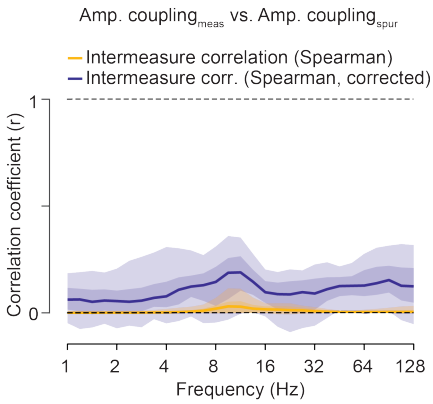

Figure A3. Non-parametric correlation between spurious and measured amplitude coupling patterns

Lines indicate median attenuation corrected (blue) and uncorrected (yellow) correlation. Shaded areas indicate the 5-95% and 25-75% inter-percentile range over space.

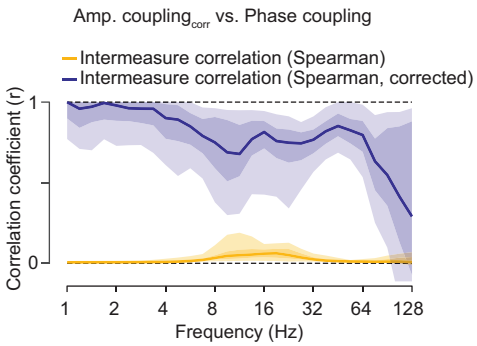

Figure A4. Non-parametric correlation between corrected amplitude coupling and phase coupling patterns

Lines indicate median attenuation corrected (blue) and uncorrected (yellow) correlation. Shaded areas indicate the 5-95% and 25-75% inter-percentile across cortical space.

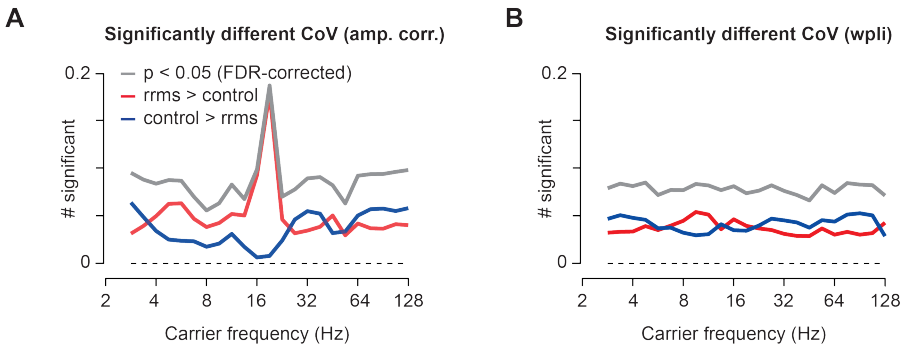

Figure A5. Comparison of variance between patients and controls

Significantly different coefficient of variation, with two-tailed Mann-Whitney U-test, between Multiple Sclerosis patients and healthy controls for every connection and frequency for (**A**) orthogonalized amplitude correlations and (**B**) weighted phase lag index. The gray line indicates all significantly different connections ($p<0.05$, FDR-corrected). The red and the blue lines specify how many connections in the patient group are increased or decreased ($p<0.05$, FDR-corrected), respectively.